Light absorption properties and potential sources of particulate brown carbon in the Pearl River Delta region of China

Zhujie Li[1,2], Haobo Tan[2]*, Jun Zheng[1]*, Li Liu[2,3], Yiming Qin[4], Nan Wang[2], Fei Li[2], Yongjie Li[5], Mingfu Cai[3], Yan Ma[1], and Chak K. Chan[4]

[1]Collaborative Innovation Center of Atmospheric Environment and Equipment Technology, Nanjing University of Information Science and Technology, Nanjing, China
[2]Key Laboratory of Regional Numerical Weather Prediction, Institute of Tropical and Marine Meteorology, China Meteorological Administration, Guangzhou, China
[3]Department of Atmospheric Science, Sun yat-sen University, Guangzhou, China
[4]School of Energy and Environment, City University of Hong Kong, Hong Kong, China
[5]Department of Civil and Environmental Engineering, Faculty of Science and Technology, University of Macau, Macau, China

Correspondence to: Haobo Tan (hbtan@grmc.gov.cn) and Jun Zheng (zheng.jun@nuist.edu.cn)

Abstract:

Brown carbon (BrC) is a special type of organic aerosols (OA), capable of absorbing solar radiation from near-ultraviolet (UV) to visible wavelengths, which may lead to an increased aerosol radiative effect in the atmosphere. While high concentrations of OAs have been observed in the Pearl River Delta (PRD) region of China, the optical properties and corresponding radiative forcing of BrC in the PRD are still not well understood. In this work, we conducted a set of comprehensive measurements of atmospheric particulate matter from 29 November 2014 to 2 January 2015 to investigate aerosol compositions, optical properties, source origins and radiative forcing effects at a suburban station in Guangzhou. The particle absorption Ångström exponent (AAE) was deduced and utilized to differentiate light absorption by BrC from that by black carbon (BC). The results showed that the average absorption contributions of BrC were 34.1±8.0% at 370 nm, 23.7±7.3% at 470 nm, 16.0±6.7% at 520 nm, 13.0±5.4% at 590 nm and 8.7±4.3% at 660 nm. A sensitivity analysis of the evaluation of the absorption Ångström exponent of BC (AAE_{BC}) was conducted based on the Mie theory calculation assuming that the BC-containing aerosol was mixed with the core-shell and external configurations. The corresponding uncertainty in AAE_{BC} was acquired. We found that variations in the imaginary refractive index (RI) of the BC core can significantly affect the estimation of AAE_{BC}. However, AAE_{BC} was relatively less sensitive to the real part of the RI of the BC core and was least sensitive to the real part of the RI of the nonlight absorbing shell. BrC absorption was closely related to aerosol potassium cation content (K^+), a common tracer of biomass burning emissions, which was most likely associated with straw burning in the rural area of the western PRD. Diurnal variation in BrC absorption revealed that primary organic aerosols had a larger BrC absorption capacity than secondary organic aerosols (SOAs). Radiative transfer simulations showed that BrC absorption may cause 2.3±1.8 W m^{-2} radiative forcing at the top of the atmosphere (TOA) and contribute to 15.8±4.4% of the aerosol warming effect. A chart was constructed to conveniently assess the BrC radiative forcing efficiency in the studied area with reference to certain aerosol single-scattering albedo (*SSA*) and BrC absorption contributions at various wavelengths. Evidently, the BrC radiative forcing efficiency was higher at shorter wavelengths.

Keywords: Brown carbon, Black carbon, Absorption Ångström exponent, Radiative forcing, Pearl River Delta.

1 Introduction

Black carbon (BC) and organic carbon (OC) are dominant carbonaceous aerosol components that mainly originate from biomass burning in a global scale (Bond et al., 2004) and have attracted great environmental concerns in rapidly developing regions. Carbonaceous aerosols can not only exert adverse impacts on public health, similar to other particulate matters, but also significantly affect the terrestrial radiation balance with enormous uncertainties. In previous studies, BC was often considered to be the only light-absorbing species (Andreae and Gelencser, 2006), and OC was believed to only be able to scatter light, i.e., causing a cooling effect (Bond et al., 2011). Nevertheless, it has been reported that some fraction of organic aerosols (OAs) may also specifically contribute to light absorption from the near-ultraviolet (UV) to visible wavelength range, which is referred to as brown carbon (BrC) (Kirchstetter et al., 2004). BrC optical properties are strongly affected by its chemical composition and physical structure, which are related to different BrC sources. BrC can originate not only from direct emissions, including smoldering, biomass burning or any type of incomplete fuel combustion process (T. C. Bond et al., 1999;Cheng et al., 2011), but also from secondary organic aerosol formation processes, such as aqueous phase reactions in acidic solutions (Desyaterik et al., 2013) or volatile organic compound (VOC) oxidation (Laskin et al., 2015;Sareen et al., 2010). In addition, BrC could have a complicated molecular composition and intermix with other substances, such as BC, non-absorbing OAs and other inorganic materials, making it complicated to investigate BrC optical properties.

BC absorption is commonly assumed to be covering the full wavelength-range. However, the light absorption property of BrC is believed to be more wavelength-dependent, which can be represented by distinct absorption Ångström exponent (AAE) values, i.e., the power exponent of the light absorption coefficient. A typical threshold for the AAE of BC (AAE_{BC}) of 1.6 has been recommended to distinguish BrC from BC (Lack and Cappa, 2010), and the AAE of BrC has been reported as having a wider range (2 to 7) (Hoffer et al., 2005). Based on the difference in the wavelength dependence of light absorption between BC and BrC, previous studies have

applied the AAE method to differentiate light absorption by BrC through multiwavelength optical measuring apparatus, such as 3-wavelength Photoacoustic Soot Spectrometer (PASS-3) (Lack and Langridge, 2013), multiwavelength Aethalometer (Olson et al., 2015), etc. Based on the AAE method, the BrC absorption contribution has been estimated to be approximately 6 to 41% of total aerosol light absorption at short wavelengths, e.g., at 370 nm and 405 nm (Washenfelder et al., 2015). A uniform AAE_{BC} from ~300 nm up to ~700 nm (Moosmüller et al., 2011) is commonly used when evaluating the BrC absorption contribution using the AAE method. However, it has been reported that the AAE_{BC} can be influenced by the mixing state, BC core size and morphology (Lack and Cappa, 2010). The lensing effect of the coating shell may enhance BC light absorption, the magnitude of which may also depend on wavelength and can alter the value of AAE_{BC} (Liu et al., 2018). Moreover, different values of AAE_{BC} have been found in the near-infrared and UV ranges (Wang et al., 2018). Therefore, using the default value of $AAE_{BC} = 1$ may lead to uncertainty in BrC absorption coefficient estimation.

Quantifying BrC optical absorption accurately is essential to interpret aerosol optical depth (AOD), and the corresponding aerosol direct radiative forcing (DRF) on the atmosphere can also be evaluated if the single-scattering albedo (*SSA*) and extinction coefficient of aerosols are known. The estimation of the DRF of BrC has shown a distinct seasonal variation, indicating the influence of different absorption properties of BrC (Arola et al., 2015). A global simulation study indicated that the average warming effect at the TOA caused by BrC absorption can be up to 0.11 W m^{-2}, corresponding to ~25% of that predicted from BC absorption only (Feng et al., 2013).

During the last three decades, rapid economic development has led to severe air pollution problems in the PRD region (Chan and Yao, 2008). With rapid increases in the automobile population and factories, high loadings of SOAs have often been observed (Tan et al., 2016b). Biofuel usage may also play a significant role during wintertime air pollution events in the PRD, indicating that the contribution from BrC light absorption cannot be ignored (Wu et al., 2018). Recently, BrC light absorption has been quantified by Qin et al. (2018) using the AAE method in the PRD region. OA chemical composition was simultaneously measured by a high-resolution time-of-flight aerosol mass spectrometer, and it was found that organic aerosols originating from biomass burning possessed the most intense absorption capability and were

105 largely responsible for BrC absorption. Qin et al. (2018) also suggested that correlations
106 between OA chemical compositions and BrC absorption were wavelength-dependent.
107 In this paper, we applied the homologous AAE differentiation method to quantify the fraction
108 of aerosol light absorption by BrC using the measurements from a seven-wavelength
109 Aethalometer. The potential error incurred with this methodology was determined using Mie
110 theory simulations, especially for various complex refractive indexes of the BC core and the
111 coating material. The correlation between BrC light absorption and water-soluble ions, which
112 is used as the source tracer, was employed to identify potential BrC sources. An atmospheric
113 radiative transfer model has also been applied to evaluate the impact of BrC on direct radiative
114 forcing using surface-based aerosol optical properties and satellite-based surface-albedo data.
115 The magnitudes of aerosol radiative forcing at the top of the atmosphere due to BC and BrC
116 were also individually quantified.

117 **2 Methodology**

118 **2.1 Sampling site**

119 Field observations were conducted at the Panyu station (113°21′E, 23°00′N), which is a
120 monitoring site of the Chinese Meteorological Administration (CMA) Atmospheric Watch
121 Network (CAWNET) that is located on the summit of Dazhengang Mountain (approximately
122 150 m above sea level) in Guangzhou, China. Figure 1 shows the location of the Panyu site,
123 which is situated at the center of the PRD and is separated from residential areas by at least 500
124 m. Some agricultural fields can be found to the west of the site. Although there were no
125 significant pollution sources nearby, this suburban site was strongly affected by pollutants
126 transported from the urban area of Guangzhou and crop residual fires transported from the rural
127 area of the PRD. The field campaign was conducted from 29 November 2014 to 2 January 2015.
128 During the measurement period, aerosol light scattering and extinction, BC concentration,
129 particle number size distribution (PNSD), OC concentration, and the water-soluble ion
130 concentrations of $PM_{2.5}$ were continuously monitored.

131 **2.2 Measurements and data analysis**

132 All instruments were housed inside the 2nd floor measurement room of a ~5-m tall, 2-story
133 building. The ambient sample was taken on the roof by a 2-m long, 12.7-mm OD stainless steel
134 inlet, and a $PM_{2.5}$ cyclone sampler was also used. The metal tubing was thermally insulated and

maintained at a constant temperature of ~25°C. A diffusion drier was also used in-line to dry the relative humidity (RH) of the air sample below 30% before further analysis.

2.2.1 Measurements of relevant species

A TSI-3936 scanning mobility particle sizer (SMPS) and a TSI-3321 aerodynamic particle sizer (APS) were utilized to measure the 10 to 500 nm mobility diameter and 0.5 to 2.5 μm aerodynamic diameter of the PNSD, respectively. The aerodynamic diameters of the APS data were converted into mobility diameters using a material density of 1.7 g cm^{-3}. A detailed data merging method has been described by Cheng et al. (2006). Furthermore, the pipe diffusion loss of SMPS has been corrected using the empirical formula proposed by Kulkarni et al. (1996). An AE-33 Aethalometer (Magee Scientific Inc.) was utilized for BC mass concentration measurement, which was derived from optical attenuation using a mass absorption cross section (MAC) of 7.77 m^2 g^{-1} at 880 nm. The sensitivity of AE-33 was approximately 0.03 μg m^{-3} for a 1-min time resolution and a 5.0 liter per minute (LPM) sample flow rate.

The $PM_{2.5}$ mass concentration was measured by an Environment Dust Monitor (Model EDM180, GRIMM Inc.), which monitored the mass concentration of $PM_{2.5}$ and PM_{10} simultaneously.

Water-soluble ions (potassium (K^+), calcium (Ca^{2+}), magnesium (Mg^{2+}), chloride (Cl^-), sulfate (SO_4^{2-}), nitrate (NO_3^-), and ammonium (NH_4^+) were measured with the Monitor for AeRosols and Gases in Air (MARGA) (Model ADI2080, Metrohm Inc.), which is an online analyzer for semi-continuous measurements of gases and water-soluble ions in aerosols (Li et al., 2010). The MARGA was automatically calibrated with standard internal solutions during field measurement. The MARGA utilized its own $PM_{2.5}$ sampling system provided by the manufacturer.

The OC mass concentration was measured by a Sunset online OC/EC analyzer (Model RT-4) with a laser transmittance-based charring correction (Wu et al., 2018). The sample flow rate of the OC/EC analyzer was maintained at 8 LPM. For each measurement cycle (one hour), samples were collected onto a quartz filter within the first 45 min and then thermal-optically analyzed during the remaining 15 min. First, OC was completely volatized in oxygen-free helium with a stepwise ramped temperature (600 °C and 840 °C). In the second stage, the temperature was reduced to 550 °C, and then EC and pyrolyzed carbon (PC) were combusted

in an oxidizing atmosphere (10% oxygen in helium), while the temperature was increased up to 870 °C step by step. The CO_2 converted from all of the carbon components was then quantified by a nondispersive infrared absorption CO_2 sensor (Lin et al., 2009). An internal calibration peak made by 5% methane in helium was applied to quantify OC and EC. To correct the PC converted from OC to EC, a tunable pulsed diode laser beam was used to monitor the laser transmittance through the quartz filter throughout the thermal-optical analysis (Bauer et al., 2012).

2.2.2 Measurements of optical properties

Light extinction by aerosols at 532 nm was detected using a cavity ring-down aerosol extinction spectrometer (CRDS) (Model XG-1000, Hexin Inc.) by measuring the decay times of laser intensity through the aerosol-containing sample and the filtered background air sample under the same conditions. The extinction coefficient (σ_{ext}) was calculated using the procedure described by Khalizov et al. (2009).

Aerosol total scattering (σ_{sp}) was measured by a TSI-3563 integrated nephelometer at three wavelengths (i.e., 450 nm, 550 nm, and 700 nm) and was calibrated with CO_2 following the manual instructions. Particle free air was used to check the nephelometer background signal once every two hours. The scattering coefficients at other wavelengths were extrapolated using the following equations:

$$SAE = -\frac{ln\left(\sigma_{scat,\lambda_0}\right) - ln\left(\sigma_{scat,550nm}\right)}{ln(\lambda_0) - ln(550)} \quad (1)$$

$$\sigma_{scat}(\lambda) = \sigma_{scat}(550) \cdot \left(\frac{\lambda}{550}\right)^{-SAE} \quad (2)$$

where λ_0=450 nm is for wavelengths less than 550 nm and λ_0=700 nm is for wavelengths greater than 550 nm. The corresponding time series of extinction coefficients, scattering coefficients, and SSA at 532 nm was displayed in Fig. S1.

The Aethalometer is also used for multi-wavelength light absorption measurements in this study. The seven-wavelength aerosol light attenuation coefficients (σ_{ATN}) were converted into aerosol light absorption coefficients (σ_{abs}) using Eq. (3) (Coen et al., 2010), where k is the parameter that accounts for the loading effect, ATN is the light attenuation through the filter with sample loading and C_{ref} is a fixed multiple scattering parameter.

$$\sigma_{abs} = \frac{\sigma_{ATN}}{(1 - k \cdot ATN) \cdot C_{ref}} \quad (3)$$

The real-time *k* value was retrieved using the dual-spot loading correction algorithm developed by Drinovec et al. (2015). The detailed formula of ATN can also be found in Drinovec et al. (2015). C_{ref} is considered a constant that strongly depends on the filter matrix effect. However, some studies have suggested that C_{ref} may vary with wavelength (Arnott et al., 2005;Segura et al., 2014). For internal combustion engines and biomass burning, C_{ref} at 370 nm was expected to be approximately 12% and 18% less than C_{ref} at 532 nm for the aerosol component, respectively (Schmid et al., 2006). Different ambient observations also showed that C_{ref} may have regional specificity, even though it was retrieved by the same methodology (Coen et al., 2010). In this study, C_{ref} =3.29 was used in Eq. (3) at each wavelength, and this value was derived from the slope of σ_{ATN} measured by the Aethalometer vs. σ_{abs}, which was deduced from the CRDS and nephelometer measurements. This C_{ref} was also very similar to the C_{ref} of 3.48 determined from an inter-comparison study between an Aethalometer and a photoacoustic soot spectrometer during a field campaign conducted in the PRD region in 2004 (Wu et al., 2009).

The BC light absorption at certain wavelengths was derived from the absorption coefficient σ_{abs} according to Beer-Lambert's law, and its variation between different pairs of wavelengths (i.e., $\sigma_{abs,BC,\lambda}$) is denoted by the absorption Ångström exponent (AAE) equation developed by Ångström (1929):

$$\sigma_{abs,BC,\lambda} = \sigma_{abs,BC,\lambda_0} \times (\lambda_0 / \lambda)^{-AAE_{BC}} \quad (4)$$

It has been suggested that the AAE of BC may vary between short and long wavelength ranges (Lack and Cappa, 2010); hence, applying a wavelength-independent AAE_{BC} may lead to uncertainties in the BC absorption calculation from one wavelength to another. In this work, the light absorptions of BC at various wavelengths were retrieved by a modified wavelength-dependent AAE differentiation method conducted by Wang et al. (2018):

$$\sigma_{abs,BC,\lambda_1} = \sigma_{abs,BC,,880nm} \times \left(\frac{880}{\lambda_1}\right)^{AAE_{BC,520\text{-}880nm}} \quad (5.1)$$

$$\sigma_{abs,BC,\lambda_2} = \sigma_{abs,BC,880nm} \times \left(\frac{880}{520}\right)^{AAE_{BC,520\text{-}880nm}} \times \left(\frac{520}{\lambda_2}\right)^{AAE_{BC,370\text{-}520nm}} \quad (5.2)$$

Here, $\sigma_{abs,BC,\lambda_1}$ represents the absorption coefficient due to only BC greater than 520 nm, and $\sigma_{abs,BC,\lambda_2}$ represents the absorption coefficient of BC less than 520 nm. $AAE_{BC,\lambda_i\text{-}\lambda_{i+1}}$ (i=1, 2 and 3) represents the AAE of BC between a longer and shorter wavelength at λ_i=880, 520 and 370 nm and was calculated as:

$$AAE_{BC,\lambda_i-\lambda_{i+1}} = -\frac{ln(\sigma_{abs,BC,\lambda_i}) - ln(\sigma_{abs,BC,\lambda_{i+1}})}{ln(\lambda_i) - ln(\lambda_{i+1})} \quad (6)$$

Accordingly, BrC absorption at a certain wavelength λ ($\sigma_{abs,BrC,\lambda}$) was equal to the value of total aerosol absorption ($\sigma_{abs,\lambda}$) minus BC absorption ($\sigma_{abs,BC,\lambda}$):

$$\sigma_{abs,BrC,\lambda} = \sigma_{abs,\lambda} - \sigma_{abs,BC,\lambda} \quad (7)$$

The light absorption data at 880 nm ($\sigma_{abs,880nm}$) were selected to represent BC absorption ($\sigma_{abs,BC,880nm}$), which shall not be affected by BrC (Drinovec et al., 2015). It has been reported that the dust-related contributions of $PM_{2.5}$ were normally less than 5% in wintertime in Guangzhou; therefore, the influence from dust could be negligible in this study (Huang et al., 2014).

2.2.3 Estimation of AAE_{BC}

Traditionally, AAE_{BC} was believed to be close to 1.0 (Bodhaine, 1995), which has been commonly used for BC measurements (Olson et al., 2015). However, studies have demonstrated that AAE_{BC} can be affected by the refractive index of coating materials, mixing state, morphology, and BC core size (Liu et al., 2015). Therefore, using the default $AAE_{BC} = 1$ may lead to uncertainty in BrC absorption estimation. To obtain the correct AAE_{BC}, a series of Mie theory calculations were conducted using a simplified core-shell model (Bohren and Huffman, 1983;Wang et al., 2018). We used a modified BHCOAT code and BHMIE code to calculate the aerosol optical properties of the core-shell and external mixture at different wavelengths (Cheng et al., 2006). In the Mie theory, a particle is taken as a perfect homogeneous sphere, and its extinction and scattering efficiencies, $Q_{ext,Mie,\lambda}$ and $Q_{scat,Mie,\lambda}$, respectively, are expressed as (Mie, 1908;Seinfeld and Pandis, 1998):

$$Q_{ext,Mie,\lambda} = \frac{2}{\alpha^2}\sum_{n=1}^{\infty}[(2n+1)Re(a_n + b_n)] \quad (8)$$

$$Q_{scat,Mie,\lambda} = \frac{2}{\alpha^2}\sum_{n=1}^{\infty}[(2n+1)(|a_n|^2 + |b_n|^2)] \quad (9)$$

where $\alpha = \pi D_p/\lambda$ is the size parameter; a_n and b_n are functions of the complex refractive index (RI) and α in the Riccati-Bessel form, respectively. *Re* in Eq. (8) denotes that only the real part of RI is taken. The absorption efficiency ($Q_{abs,Mie,\lambda}$) is thus the difference between the extinction and scattering efficiencies:

$$Q_{abs,Mie,\lambda} = Q_{ext,Mie,\lambda} - Q_{scat,Mie,\lambda} \quad (10)$$

Then, the absorption coefficient $\sigma_{abs,Mie,\lambda}$ was obtained by the following (Bricaud and Morel, 1986):

$$\sigma_{abs,Mie,\lambda} = \int Q_{abs,Mie,\lambda} \cdot (\frac{\pi}{4} D_p^2) \cdot N(\log D_p) \cdot d \log D_p \quad (11)$$

where $N(\log D_p)$ is the PNSD function. A two-component parameterization of dry particles, i.e., the BC core and the nonlight-absorbing species, was applied to calculate aerosol optical properties here (Wex et al., 2002). $\widetilde{m}_{core}$ represents the RI of the BC core, and $\widetilde{m}_{non}$ represents the RI of nonlight-absorbing particles.

In a realistic atmosphere, some nonlight-absorbing particles may exist independently without BC (Liu et al., 2013; Cheung et al., 2016). In this work, the portion of nonlight-absorbing particles at a certain size (D_p) was determined by our previous measurements at the same site using a Volatility Tandem Differential Mobility Analyzer (V-TDMA), during which completely vaporized (CV) particles at 300°C were referred to as nonlight-absorbing particles that externally mixed with other BC-containing particles. Thus, the PNSD of CV particles ($N(logD_p)_{CV}$) and BC-containing particles ($N(logD_p)_{BC}$) can be given by the following equations:

$$N(logD_p)_{CV} = N(logD_p)_{measure} \cdot \Phi(D_p)_{N,CV} \quad (12)$$

$$N(logD_p)_{BC} = N(logD_p)_{measure} \cdot (1 - \Phi(D_p)_{N,CV}) \quad (13)$$

where $N(logD_p)_{measure}$ is the PNSD of the measured particles from SMPS and APS. $\Phi(D_p)_{N,CV}$ was the number fraction of CV particles in different size bin.

A previous study applied three kinds of BC mixture models to calculate the aerosol optical properties, including external, homogenously internal and core-shell mixtures (Bohren and Huffman, 2007;Seinfeld and Pandis, 1998). To quantify the mixing state of BC, r_{ext} was defined as the mass fraction of externally mixed BC (M_{ext}) in total BC (M_{BC}):

$$r_{ext} = \frac{M_{ext}}{M_{BC}} \quad (14)$$

Tan et al. (2016) suggested that two extreme conditions of external and core-shell mixtures comprised the actual mixing state of BC in the PRD. Hence, we simply divided the PNSD of BC into the PNSD from an external mixture of BC and a core-shell mixture of BC. The PNSDs

of externally mixed BC particles and core-shell mixed BC particles were referred to by the following equations with a given r_{ext}.

$$N(logD_p)_{ext} = N(logD_p)_{BC} \cdot f_{BC} \cdot r_{ext} \quad (15)$$

$$N(logD_p)_{core-shell} = N(logD_p)_{BC} \cdot (1 - f_{BC} \cdot r_{ext}) \quad (16)$$

f_{BC} was defined as the BC volume fraction in the BC-containing particle volume, which can be converted from the BC mass concentration:

$$f_{BC} = \frac{M_{BC}}{\rho_{BC} \cdot \sum_{D_P} N(logD_p)_{BC} \cdot (\frac{\pi}{6} \cdot D_p^3)} \quad (17)$$

where ρ_{BC} is the density of BC and is assumed to be 1.5 g cm^{-3} (Ma et al., 2012); M_{BC} is the BC mass concentration derived from the multi-angle absorption photometer (MAAP), which was obtained by an empirical formula from the Aethalometer that measured the BC concentration ($M_{BC,AE}$), as proposed by Wu et al. (2009):

$$M_{BC} = 0.897 \cdot M_{BC,AE} - 0.062 \quad (18)$$

The PNSDs of externally mixed nonlight-absorbing particles and externally mixed BC particles were input into the BHMIE code, and the PNSD of the core-shell mixed particles was imported into the BHCOAT code. Another critical parameter for the core-shell model was the diameter of the BC core. For the simplified core-shell model we applied, the visualization was that a homogeneous BC core sphere was encapsulated in a shell of non-absorbing coating (Bohren and Huffman, 2007). Without size-resolved coating thickness measurements, core-shell mixed particles simply assumed that cores with the same diameter had the same coating thickness. Therefore, the diameter of the BC core was calculated as follows:

$$D_{core} = D_p \cdot (\frac{f_{BC} - f_{BC} \cdot r_{ext}}{1 - f_{BC} \cdot r_{ext}})^{\frac{1}{3}} \quad (19)$$

D_{core} and D_p are inputted as parameters into a_n and b_n, respectively, which was described by Bohren and Huffman (2007). The corresponding time series of size distribution of the derived external BC and internal BC core were illustrated in Fig. S2. Thus, the $\sigma_{abs,BC,Mie,\lambda_i}$ values of all six wavelengths were calculated through the Mie model, and then the AAE_{BC} values of those five wavelengths were obtained using Eq. (6). The performance of this empirically determined calculation method has been compared with other possible BC mixing schemes in details (see Table 1).

2.2.4 Atmospheric radiative transfer model

In this work, theSanta Barbara DISORT Atmospheric Radiative Transfer (SBDART) model was employed to estimate the DRF of BrC absorption, i.e., its effects on the downward and upward fluxes (F in W m^{-2}) of solar radiation at the TOA. SBDART is a software tool that can be used to compute plane-parallel radiative transfer under both clear and cloudy conditions within the atmosphere. More details about this model have been described by Ricchiazzi et al. (1998). Both ground measurements and remote sensing data were used in the simulation. The surface albedo was derived from a 500 m resolution MODIS BRDF/albedo model parameter product (MCD43A3, daily). The MCD43A3 products are the total shortwave broadband black-sky albedo (α_{BSA}) and white-sky albedo (α_{WSA}), while the actual surface albedo (α) was computed from a linear combination of α_{WSA} and α_{BSA}, which were weighted by the diffuse ratio (r_d) and direct ratio (1-r_d), respectively:

$$\alpha=(1 - r_d) \cdot \alpha_{BSA}+r_d \cdot \alpha_{WSA} \quad (20)$$

r_d was obtained from an exponential fit of Eq. (21) based on empirical observations (Stokes and Schwartz, 1994;Roesch, 2004):

$$r_d=0.122+0.85e^{-4.8\mu_0} \quad (21)$$

where μ_0 is the cosine of the zenith angle, which is calculated by the model for any specified date, time, and latitude and longitude of the site. The surface-based aerosol optical properties, including the aerosol light absorption coefficients of both BC and BrC, i.e., differentiated from each other under the assumption of uniform AAE_{BC}, along with the nephelometer-measured aerosol scattering coefficients, were used to calculate the *SSA* at different wavelengths according to Eq. (22),

$$SSA(\lambda)=\frac{\sigma_{scat,\lambda}}{\sigma_{abs,BrC,\lambda}+\sigma_{abs,BC,\lambda}+\sigma_{scat,\lambda}} \quad (22)$$

which was then used in the model calculation. Finally, the AOD and asymmetry factor (ASY) at 440, 675 and 870 nm were derived from the Aerosol Robotic Network (AERONET) measurements at the Hong Kong Polytechnic University site (Holben et al., 1998), which is approximately 115 km to the southeast of the Panyu site. The tropical atmospheric profile was used in the SBDART model based on the prevailing weather conditions in the PRD. The aerosol DRF (ΔF) was calculated as the difference between the downward and upward radiation fluxes:

$$\Delta F = F\downarrow - F\uparrow \quad (23)$$

3 Results and discussion

3.1 Aerosol light absorption

The AAE_{BC} is widely defined as the uniform representation of the wavelength dependence of a BC particle (Olson et al., 2015). In reality, AAE_{BC} may vary significantly with BC containing aerosols of different sizes, mixing states, and morphologies (Scarnato et al., 2013;Lack and Langridge, 2013). In fact, some studies showed that the AAE of a large-size, pure BC core may be less than 1.0 (Liu et al., 2018) and that the AAE of BC coated with a non-absorbing shell may be larger than that under uniformity (Lack and Cappa, 2010).

It has been suggested that a significant fraction of smaller size particles is non BC-containing (Ma et al., 2017;Cheung et al., 2016). BC and non-BC materials can also be externally or internally mixed. Although size resolved BC measurements were not available during this work, we have conducted size resolved Volatility Tandem Differential Mobility Analyzer (V-TDMA) measurements at 300℃ for 40, 80, 110, 150, 200 and 300 nm, respectively, during an earlier field campaign (February 2014) at the same site as in this work. At 300℃, all non-BC particle will be completely vaporized (CV) and thus the portion of non BC particles at such size, denoted as $\Phi_{N,CV}$, can be determined. The average $\Phi_{N,CV}$ values were 0.384, 0.181, 0.180, 0.158, 0.143 and 0.137, corresponding to 40, 80, 110, 150, 200 and 300 nm (see Fig. S3), respectively (Cheung et al., 2016;Tan et al., 2016a). The size-independent $\Phi_{N,CV}$ was interpolated linearly with these six diameters. For particle size larger than 300 nm and less than 40 nm, $\Phi_{N,CV}$ values were set to 0.137 and 0.384, respectively. For particle size larger than 300 nm and less than 40 nm, $\Phi_{N,CV}$ values were set to 0.137 and 0.384, respectively. Accordingly, the complete distribution of $\Phi_{N,CV}$ for the whole PNSD was obtained. The mixing states of BC particles were also estimated here, i.e., the mass portion of externally mixed BC with respect to total BC, denoted as r_{ext}. The value of r_{ext} was taken as 0.58, which was obtained using an optical closure method during a previous field experiment at this site (Tan et al., 2016a). During the following Mie theory calculation, a fixed refractive index ($\widetilde{m}_{core}$=1.80-0.54i, $\widetilde{m}_{non}$=1.55-10^{-7}i) was adopted for the whole size range. Accordingly, the calculated BC absorption at 880 nm (Abs_{880}) was 21.869 Mm^{-1}, which is reasonably close to the measured mean value of 21.199 Mm^{-1}. To further validate our calculation scheme (Base Case), we have considered several extreme cases. Case 1: BC is completely externally mixed with non-BC particles, i.e., $\Phi_{N,CV}$ = 0 and r_{ext} = 1;

Case 2: BC is present in every size bin and BC is completely internally mixed with non-BC material, i.e., $\Phi_{N,CV} = 0$ and $r_{ext} = 0$; Case 3: BC is both internally and externally mixed but there is no non BC-containing particles, i.e., $\Phi_{N,CV} = 0$ and $r_{ext} = 0.58$; Case 4: BC is internally mixed with non-BC material and there is non-BC particles present, i.e., $\Phi_{N,CV}$ ranges from 0.384 to 0.137 and $r_{ext} = 0$; Case 5: the same as case 4 except assuming a fixed non-BC to BC ratio of 0.5, i.e., $\Phi_{N,CV} = 0.5$, $r_{ext} = 0$; Case 6: the same as case 5 except that some externally mixed BC is also present, i.e., $\Phi_{N,CV} = 0.5$, $r_{ext} = 0.58$. The calculation results are listed in Table 1. Evidently, case 1 (complete externally mixed) will significantly underestimate the measured Abs_{880}, indicating that most BC particles were not likely externally mixed at the Panyu site. Complete internal mixing state (case 2, 4, and 5), on the contrary, would substantially overestimate the BC absorption regardless the form of BC core distribution function. However, when the r_{ext} were considered (case base, 3, and 6), the calculated Abs_{880} values were all very close to the measured value.

When the AAE_{BC} was assumed to be uniform, the campaign-averaged σ_{BrC} values were 17.6±13.7 Mm^{-1} at 370 nm, 9.7±7.9 Mm^{-1} at 470 nm, 5.8±5.1 Mm^{-1} at 520 nm, 4.0±3.5 Mm^{-1} at 590 nm and 2.3±2.1 Mm^{-1} at 660 nm. At the corresponding wavelengths, BrC absorption contributed 26.2±8.5%, 20.0±7.3%, 14.3±6.5%, 11.7±5.3%, and 7.8±4.1% to the total aerosol absorption, respectively. When the AAE_{BC} was applied as the result of the Mie model calculation, the corrected campaign-averaged $\sigma_{abs,BrC}$ values were 23.5±17.7 Mm^{-1} at 370 nm, 11.8±9.5 Mm^{-1} at 470 nm, 6.7±5.7 Mm^{-1} at 520 nm, 4.6±3.9 Mm^{-1} at 590 nm and 2.6±2.3 Mm^{-1} at 660 nm. At the corresponding wavelengths, BrC absorption contributed 34.1±8.0%, 23.7±7.3%, 16.0±6.7%, 13.0±5.4%, and 8.7±4.3% to the total aerosol absorption (see Fig. 2), respectively. Evidently, aerosol light absorption was predominantly due to BC; however, BrC also played a significant role, especially at shorter wavelengths. Table 2 shows the intercomparison of BrC light absorption in the near UV range between this work and other studies in the East Asian region. Clearly, the reported values vary substantially, and our result is toward the lower end of values. Figure. S4 displayed the time series of particle AAE measured by the Aethalometer and AAE_{BC} was derived from Mie model calculation. The AAE_{BC} was almost always lower than AAE, indicating appreciable BrC light absorption at the Panyu site.

3.2 Uncertainty in BC and BrC optical differentiation

Theoretically, the magnitude of BC absorptions can be affected by both parts of the complex refractive indexes (RIs); thus, AAE_{BC} may also vary with the RIs of both the BC core and coating shell. In fact, RI was also one of the least known properties of BC and other coating materials with negligible absorbing capabilities. The refractive index of the BC core ($\widetilde{m}_{core}$) displays a wide range of variations (Liu et al., 2018). Typically, the real and imaginary parts of the RI can vary from 1.5 to 2.0 and 0.5 to 1.1, respectively. In addition, the shell was assumed to consist of non-absorbing material in the core-shell model, i.e., its imaginary RI was set to be close to zero (10^{-7}). The real part of the non-absorbing material RI ($\widetilde{m}_{non}$) may vary from 1.35 to 1.6 due to the presence of OA (Zhang et al., 2018;Redmond and Thompson, 2011) and inorganic salts (Erlick et al., 2011). Hence, it is necessary to investigate the uncertainties associated with the variations in AAE_{BC} by varying the RIs of both the BC core and the non-absorbing materials.

Figure 3 shows the impacts of RI on the evaluations of AAE_{BC} based on core-shell and external configuration, where the RI of the BC core was set to be constant, i.e., $\widetilde{m}_{core}$=1.80-0.54i, and the real part of $\widetilde{m}_{non}$ varied from 1.35 to 1.6 at an interval of 0.05, with the imaginary part of $\widetilde{m}_{non}$ set at 10^{-7}. As shown in Fig. 3a, the calculated AAE_{BC} for the core-shell model was higher than 1.0 at longer wavelengths (520 to 880 nm) and lower than 1.0 at shorter wavelengths (370 to 520 nm) (the red line in Fig. 3 denotes AAE_{BC}=1). The averaged $AAE_{BC,370\text{-}520nm}$ ranged from 0.84 to 0.87, and the $AAE_{BC,520\text{-}880nm}$ ranged from 1.07 to 1.15, indicating that the $AAE_{BC,520\text{-}880nm}$ appeared to be more sensitive to the shell's real part than $AAE_{BC,370\text{-}520nm}$. Even if the shell material was assumed to be non-absorbing, the variation in the real RI of the shell, which was referred to as the real part of $\widetilde{m}_{non}$, still led to changes in the shell's refractivity and correspondingly altered its lensing effect, causing a change in AAE_{BC}. Meanwhile, $AAE_{BC,370\text{-}520nm}$ and $AAE_{BC,520\text{-}880nm}$ generally increased with an increasing real part of the shell. In Fig. 3b, under the externally mixed conditions, $AAE_{BC,370\text{-}520nm}$ and $AAE_{BC,520\text{-}880nm}$ were both less than 1.0. The average $AAE_{BC,370\text{-}520nm}$ was 0.33, and the average $AAE_{BC,520\text{-}880nm}$ was 0.63. These values were far less than the values under core-shell mixture conditions. In the external mixture model, the BC core and nonlight-absorbing materials were assumed to exist dependently, and then the optical properties of these two components were considered separately. Therefore,

altering the real part of the externally mixed non-absorbing material would not affect the light absorption property of the BC core or AAE_{BC}.

The impacts of the BC core on AAE_{BC} are shown in Fig. 4, where the refractive index of nonlight-absorbing materials was assumed to be $\tilde{m}_{non}$=1.55-$10^{-7}i$ and $\tilde{m}_{non}$ was wavelength-independent. Fig. 4 was obtained with a core-shell mixture model (Fig. 4a and 4b) and an external mixture model (Fig. 4c and 4d) by varying the real part of $\tilde{m}_{core}$ from 1.5 to 2.0 with a step of 0.05 and varying the imaginary part of the $\tilde{m}_{core}$ from 0.4 to 1.0 with a step of 0.05, respectively. As shown in Figs. 4a and 4b, for the core-shell mixture, the averaged $AAE_{BC,370-520nm}$ ranged from 0.55 to 0.99, and the averaged $AAE_{BC,520-880nm}$ ranged from 0.84 to 1.27. The AAE_{BC} at a certain wavelength generally increased when increasing the real part of $\tilde{m}_{core}$ but decreased when increasing the imaginary part of $\tilde{m}_{core}$. The AAE_{BC} appeared to be more sensitive to the imaginary part of $\tilde{m}_{core}$ than the real part of $\tilde{m}_{core}$ because the imaginary part of $\tilde{m}_{core}$ was directly related to the light-absorbing properties of particles. In Fig. 4c and 4d, for the external mixture, the averaged $AAE_{BC,370-520nm}$ ranged from 0.04 to 0.45 and the averaged $AAE_{BC,520-880nm}$ ranged from 0.28 to 0.79, while the averaged $AAE_{BC,370-520nm}$ and $AAE_{BC,520-880nm}$ were both less than 1.0. Similar to the core-shell mixture, the $AAE_{BC,520-880nm}$ increased when increasing the real part of $\tilde{m}_{core}$ but decreased when increasing the imaginary part of $\tilde{m}_{core}$. However, the variation patterns of $AAE_{BC,370-520nm}$ were different from those of $AAE_{BC,520-880nm}$. The $AAE_{BC,370-520nm}$ values were not changed by altering the real part of $\tilde{m}_{core}$ within the low imaginary part of $\tilde{m}_{core}$, whereas the $AAE_{BC,370-520nm}$ values still increased when increasing the real part of $\tilde{m}_{core}$ within the high imaginary part of $\tilde{m}_{core}$. A possible explanation was that the externally mixed BC core had weak light absorption within the low imaginary part of $\tilde{m}_{core}$, causing the $AAE_{BC,370-520nm}$ values to be insensitive to the real part of $\tilde{m}_{core}$. The $AAE_{BC,520-880nm}$ values were higher than the $AAE_{BC,370-520nm}$ values regardless of whether in they were for the core-shell mixture or external mixture. In addition, the AAE_{BC} values conducted by the core-shell mixture were higher than those conducted by the external mixture.

Figure 4 demonstrates that the variation in the imaginary RI of the BC core has the most significant impact on the estimated AAE_{BC}, indicating that the chemical component of BC emitted from different sources leads to a large uncertainty in AAE_{BC} estimation. At the same time, the influence arising from varying the real RI of the BC core was relatively moderate.

Nevertheless, Fig. 3 demonstrated that change in the real RI of the non-absorbing materials caused the least/no impact compared to that caused by the variations in the complex RI of the BC core.

It should be pointed out that most BC-containing particles are often observed as fractal rather than spherical in shape (Katrinak et al., 1993). Because the Mie model assumes that all particles are spherical, it may lead to potential uncertainty for the estimation of AAE_{BC} and BrC absorption contributions. Moreover, the externally mixed soot aggregates were "chain-like" or "puff-like" in the PRD dry season (Feng et al., 2010), in which the fractal dimension (D_f) was between 1.5 and 2.0. Coating soot aggregates were likely sphere (D_f approaches 3) from the high-resolution transmission electron microscopy (TEM) measurements taken in Hongkong ((Zhou et al., 2014)). A soot aggregate sensitivity study with the superposition T-matrix method indicated that using the assumption of volume-equivalent spheres for the soot aggregates may result in an overestimation of approximately up to 15% and an underestimation of approximately up to 50% in the predicted 870 nm light absorption when the D_f is between 1.5 and 3.0 (Liu et al., 2008). However, it should be recognized that the complex shapes or positions of the BC core inside the particle make it impractical to be numerically simulated in the exact details. By far the Mie model with a core-shell configuration would be the most practical and effective simulation scheme for BC particle optical property simulation.

Furthermore, we have performed Monte Carlo simulations to evaluate the uncertainties of the Mie calculation performed during this work. In the simulation, a sequence of random numbers or errors were applied to the input parameters, and then the corresponding uncertainties of particle light absorption and AAE_{BC} by were computed using the Mie model. Five hundred of reiteration were conducted during the simulation such that the random errors will be normally distributed. The standard deviations (σ) of all input parameters are listed in Table S1. In order to cover the effect of extreme value, we used a range of $\pm 3\sigma$, or a confidence level of 99%, in the Mont Carlo simulation. Table S2 listed the Monte Carlo simulation results, i.e., the average relative standard deviations (σ_{Mie}) of the calculated BC light absorption at 880 nm (Abs_{880}), $AAE_{BC,370-520}$, and $AAE_{BC,520-880}$. The uncertainties of the calculated Abs_{880}, $AAE_{BC,370-520}$, and $AAE_{BC,520-880}$ at 2 times of σ_{Mie}, i.e., at a confidence coefficient of 95%, were approximately $\pm 31\%$, $\pm 16\%$, and $\pm 13\%$, respectively. Figure S5 also showed the time series of the uncertainties

of Abs_{880}, $AAE_{BC,370-520}$ and $AAE_{BC,520-880}$ from Monte Carlo simulation for the campaign period.

3.3 Characteristics of BrC light absorption, water-soluble ions and OC concentrations

Globally, BrC has been observed to be highly correlated with biomass and biofuel burning emissions (Laskin et al., 2015). Since large quantities of sylvite are present in biomass burning particles, the K^+ abundance has often been used as a biomass burning tracer (Levine, 1991). Figure 5 presents the time series of the OC mass concentration, K^+ concentration, and BrC absorption from 29 November 2014 to 2 January 2015 at the Panyu site. The range of the OC concentration obtained from the OC/EC online analyzer was from 1.5 to 65.2 μg $cm^{-3,}$ and the campaign average was 12.5±7.3 μg cm^{-3}. The BrC absorption hourly mean data were between 0.2 and 123.2 $Mm^{-1,}$ and the campaign average was 23.5±17.7 Mm^{-1}. On the other hand, the average K^+ concentration was 1.0 ± 0.7 μg cm^{-3} (ranging from 0 to 5.4 μg cm^{-3}). Clearly, similar trends among OC, K^+, and BrC absorption can be seen during this field campaign (Fig. 5).

To investigate the origins of these observed OC, K^+, and BrC, wind rose plots (as shown in Fig. 6) were generated for OC, K^+, and BrC absorption, respectively. All three panels of Fig. 6 consistently show that the three substances were associated with the same wind pattern. For the entire campaign period, the highest values of OC, K^+, and $\sigma_{abs,BrC,370nm}$ were mostly associated with southwesterly winds with a relatively low wind speed (~2 m s^{-1}). The relatively higher OC and K^+ concentrations were highly related to the seasonal straw burning in the countryside of the PRD located to the west of the Panyu station. In contrast, OC and K^+ concentrations during periods with easterly winds were substantially lower than those during periods with westerly winds. The wind rose plot of $\sigma_{abs,BrC,370nm}$ is shown in Fig. 6c. Similar to OC and K^+, $\sigma_{abs,BrC,370nm}$ showed higher values under weak (<2 m s^{-1}) westerly winds and lower values from the north and south, indicating that BrC absorption was likely attributed to local sources and was accumulated under calm wind conditions. Figure S6 showed the 3-day backward trajectory and the fire counts for 5 to 7 (Fig. S6a), 12 to 14 (Fig. S6b) and 24 to 26 (Fig. S6c) in November 2014, representing low loading, moderate loading and high loading period. Clearly, the high loading period concurred with stagnant air movement and higher fire counts, indicating the contribution from open fire burning sources. However, there was a detectable difference among the three rose plots of Fig. 6 in the maximum concentration direction. A possible explanation was that although biomass burning emissions were believed to be the dominant and primary

source of OC, K^+, and BrC, their emission ratios were highly variable and may change with the type of biofuel and burning condition and may even vary during different stages of burning (Burling et al., 2012). Although biomass burning emissions contain substantial light-absorbing BrC, further atmospheric aging processes may significantly reduce its light-absorbing capability (Satish et al., 2017). Moreover, secondary formation may also lead to BrC formation inside these primary aerosols, such as humic-like substances formed through aqueous-phase reactions, which have been suggested to be an important component of BrC (Andreae and Gelencser, 2006).

To further explore the possible sources of BrC optical absorption, the diurnal variations in OC, K^+, $\sigma_{abs,BrC,370nm}$, and $\sigma_{abs,BrC,370nm}$ /OC values are plotted in Fig. 7. The diurnal variation in OC at the Panyu site appeared to be dominated by the development of the planetary boundary layer (PBL) height, i.e., primary emissions accumulated at night and were swiftly diluted by vertical mixing in the morning. The slight increase in OC in the afternoon indicated that photochemistry may have still weakly contributed to SOA formation. Fig. 7b shows the diurnal variation in K^+. Unlike OC, K^+ shows a small peak at approximately 6 AM, which was consistent with breakfast time and was very likely due to cooking activities using biofuel. No lunch and dinner time K^+ peaks were observed. The most likely explanation is that the boundary layer height is much higher during lunch and dinner time than in the early morning, providing a much better atmospheric diffusion condition for air pollutants. It is still a common practice to collect straw as biofuel in local rural areas, which can be visually spotted but is not heavily utilized in the region. However, the diurnal profile of $\sigma_{abs,BrC,370nm}$ (see Fig. 7c) shows the combined features of OC and K^+ since both primary and secondary processes affect its intensity. The nighttime increasing trend was most likely attributed to straw burning activities in early winter in nearby rural areas that continued to accumulate within the shallow PBL (Jiang et al., 2013). $\sigma_{abs,BrC,370nm}$/OC, i.e., the mass absorption coefficient of BrC (MAC_{BrC}) (Fig. 7d), showed a relatively flat pattern, with a pronounced dip in the afternoon and higher values at nighttime, which was likely due to enhanced primary emissions and stable stratification at nighttime. Declining trends during the late morning and afternoon hours indicated that the aging process and photochemical production may reduce the light-absorbing capacity of BrC (Qin et al., 2018).

546 Furthermore, Fig. 8 shows the linear regression analysis results used to evaluate the correlations
547 of $\sigma_{abs,BrC,370nm}$ with the OC, K^+, Ca^{2+}, Mg^{2+}, Cl^-, SO_4^{2-}, NO_3^-, and NH_4^+ concentrations. The best
548 correlations can be found between $\sigma_{abs,BrC,370nm}$ and K^+ (R^2=0.6148), followed by those between
549 $\sigma_{abs,BrC,370nm}$ and OC (R^2=0.4514), NO_3^- (R^2=0.4224) and NH_4^+ (R^2=0.4656). Source
550 apportionment analysis of OA and BrC absorption in Beijing and Guangzhou illustrated that
551 biomass burning organic aerosols (BBOAs) correlated well with BrC light absorption (Xie et
552 al., 2018;Qin et al., 2018). Thus, the significant correlation between BrC absorption and K^+
553 reaffirmed that biomass burning was the crucial emission source of BrC observed in this work.
554 Although the geographic location of the observation site was situated in a coastal area and K^+
555 could also be found in sea salt (Pio et al., 2008), it should be noted that the prevailing wind
556 direction during winter was from the north (see Fig. 3), which drives maritime air parcels away
557 from the site. Hence, the effect of sea salt and crustal materials to K^+ was slight, which was
558 demonstrated in the supplementary information as shown in Fig. S8. Other earlier studies also
559 suggested that the sea salt contribution to the K^+ concentrations of $PM_{2.5}$ was trivial in the PRD
560 region during the winter (Lai et al., 2007). Another possible K^+ source was coal combustion.
561 The coal consumption in the PRD region was dominated by coal-fired power plants. The
562 emission from power plants was usually very steady and was less likely to affect the diurnal
563 correlation between K^+ and BrC absorption. As shown in Fig. S7, the ratios of $K^+/PM_{2.5}$ varies
564 approximately from 0.015 and 0.020 and the diurnal profile of $K^+/PM_{2.5}$ shows very little
565 variation. Yu et al. (2018) have suggested that K^+ usually accounted for 2.34-5.49% of $PM_{2.5}$ in
566 the laboratory biomass burning study. However, K^+ was normally lower than 1% of coal
567 combustion $PM_{2.5}$. Therefore, the ratio range of K^+ to $PM_{2.5}$ observed in this work likely
568 indicated aged biomass burning particles. Both nitrogen oxides (NO_x) and ammonia (NH_3) can
569 be found in biomass burning plumes (Andreae and Merlet, 2001). For NO_3^- and NH_4^+, nitrate
570 can be converted from NO_x through atmospheric reactions, and ammonium may originate from
571 NH_3. However, similar to the diurnal variation in $\sigma_{abs,BrC,370nm}$, diurnal variations in NH_4^+ and
572 NO_3^- also increased in the afternoon and appeared at nighttime in Fig S7. However, $NO_3^-/PM_{2.5}$
573 and $NH_4^+/PM_{2.5}$ reached their peaks at noon, indicating that ammonium nitrate formed from the
574 secondary reaction at this time. Along with the reduced boundary layer height and ambient
575 temperature, NO_3^- was accumulated until the photochemical reaction stopped at night. The

diurnal variation in NH_4^+ was similar to that in NO_3^- due to the acid/base neutralization reaction. The overlapping of the $\sigma_{abs,BrC,370nm}$, NH_4^+ and NO_3^- diurnal variations would lead to a significant correlation between BrC absorption and NO_3^- or NH_4^+. High concentrations of Ca^{2+} and Mg^{2+} are often found in dust-related aerosols (Lee et al., 1999). $\sigma_{abs,BrC,370nm}$ showed poor correlations with both Ca^{2+} and Mg^{2+}, indicating that dust-related aerosol components contribute insignificantly to the total aerosol mass loading and, thus, dust may not affect the AAE differentiation method used in this work. Although sulfur dioxide (SO_2) may also be emitted by biomass burning, SO_4^{2-} is often believed to be secondary in nature, and the presence of other intense SO_2 sources (e.g., automobile and industrial emissions) further reduces the correlation between BrC and SO_4^{2-}. Sources of Cl^- include both combustion and sea salt spray (Waldman et al., 1991). Although the prevailing wintertime wind direction was from the north, sea salt can still be carried to the site by a weak sea breeze, and thus, Cl^- may not show considerable correlation with BrC.

3.4 BrC radiative forcing efficiency

The radiative effects of aerosol scattering, BrC absorption, and BC absorption were investigated by the SBDART model. For each investigated variable under cloud-free conditions, we run the model twice to calculate the DRF at the TOA with and without the investigated variable. Accordingly, the difference of ΔF between the two simulations was considered as the radiative effect of the investigated variable. The results showed that the average radiative forcings at the TOA by scattering, BrC absorption, and BC absorption were -21.4±5.5 W m^{-2}, 2.3±1.8 W m^{-2}, and 10.9±5.1 W m^{-2}, respectively. Furthermore, BrC absorption was attributed to 15.8±4.4% of the warming effect caused by aerosol light absorption, demonstrating the nonnegligible role of BrC in radiative forcing evaluation.

We also calculated the BrC radiative forcing efficiency (RFE) under various *SSA* (ranging from 0.7 to 0.99) at three wavelengths, i.e., 440 nm, 675 nm, and 870 nm. The RFE was denoted as the radiative forcing normalized by the AOD. The average AOD and ASY at the three wavelengths were 0.365 and 0.691 at 440 nm, 0.212 and 0.632 at 675 nm, and 0.154 and 0.619 at 870 nm, respectively. A solar zenith angle of 55° and an average shortwave broadband surface albedo (0.119) were used in the calculation. The results were plotted as a set of RFE lookup charts as a function of the surface BrC absorption contribution (see Fig. 9).

In general, for any wavelength, the RFE increased with increasing BrC absorption contribution for a certain *SSA*, indicating that BrC was a more efficient radiative forcing agent due to the preferential absorbance of BrC in a shorter wavelength range. However, for a certain BrC absorption contribution, the RFE increased with decreasing *SSA*, i.e., a higher portion of light-absorbing aerosol components can lead to more efficient radiative forcing. The trend among panels (a), (b), and (c) in Fig. 9 demonstrated that the effect of BrC absorption contribution on RFE was wavelength-dependent, i.e., BrC was a weaker radiative forcing agent at longer wavelengths, which is also consistent with the wavelength-dependent light-absorbing property of BrC. The red stars in Fig. 9 denote the average *SSA* and BrC absorption contribution conditions during this campaign, i.e., 0.029 W m^{-2} per unit AOD at 440 nm (Fig. 9a), 0.007 W m^{-2} per unit AOD at 675 nm (Fig. 9b), and 0.0002 W m^{-2} per unit AOD at 870 nm (Fig. 9c). These results suggested that the average value of RFE decreased distinctly from 440 nm to 870 nm not only because of the lower BrC absorption contribution but also because of the wavelength-dependence of the BrC RFE. It should also be noted that the simulations were based on *SSA* measured under dry conditions. Under the typical ambient conditions of the PRD, the *SSA* might be markedly enhanced by aerosol water uptake (Jung et al., 2009), and then, the BrC radiative forcing efficiency might be less. Moreover, Fig. 9 also serves as a lookup table to conveniently assess the BrC radiative forcing efficiency at different wavelengths with different BrC absorption contributions for a certain *SSA*.

4 Conclusion

In this work, light absorption due to BrC in the PRD region of China was quantitatively deduced during the winter season of 2014. The AAE of ambient particles and BC core were derived from the measurements. For ambient particles, $AAE_{370\text{-}520nm}$ and $AAE_{520\text{-}880nm}$ ranged from 0.81 to 2.31 and 0.91 to 2.13, respectively. In the case of BC, $AAE_{BC,370\text{-}520nm}$ and $AAE_{BC,520\text{-}880nm}$ ranged from 0.59 to 0.98 and 0.82 to 1.15, respectively. Using the absorption coefficients of BC calculated according to the Mie theory and the observed total aerosol absorption coefficients, we estimated the AAE_{BC} and hence the BrC absorption contribution for the optically equivalent mixture configuration. The average BrC light absorption contribution ranged from 8.7±4.3% at 660 nm up to 34.1±8.0% at 370 nm when AAE_{BC} was set as uniform. The sensitivity of AAE_{BC} estimation associated with different RI and mixing state assumptions was further investigated.

The results showed that variations in the real RI of the non-absorbing material (1.35 to 1.6) may decrease $AAE_{BC,370\text{-}520nm}$ from 0.84 to 0.87 and $AAE_{BC,520\text{-}880nm}$ from 1.07 to 1.15 for core-shell mixtures, with an $AAE_{BC,370\text{-}520nm}$ of 0.33 and $AAE_{BC,520\text{-}880nm}$ of 0.63 for external mixtures. Variations in the core's real RI (1.5 to 2.0) and imaginary RI (0.4 to 1.0) may reduce $AAE_{BC,370\text{-}520nm}$ from 0.55 to 0.99 and $AAE_{BC,520\text{-}880nm}$ from 0.84 to 1.27 for the core-shell mixture and reduce $AAE_{BC,370\text{-}520nm}$ from 0.04 to 0.45 and $AAE_{BC,520\text{-}880nm}$ from 0.28 to 0.79 for the external mixture. These results indicate that the optical properties of the BC core and non-absorbing material can significantly affect the accuracy of AAE_{BC} and corresponding BrC absorption contribution estimations. Compared to the values of BrC light absorption coefficient and BrC light absorption contribution from other similar studies conducted in the East Asia region, the BrC measured in this work showed relatively lower values of light absorption coefficient but was found responsible for relatively higher portion of light absorption.

Additionally, the measurements of major water-soluble inorganic ions (including K^+, NO_3^-, and NH_4^+) and particulate OC showed consistent features with those of $\sigma_{abs,BrC,370nm}$, implying that BrC was associated with biomass-burning emissions from nearby rural areas. Moreover, the diurnal trend in $\sigma_{abs,BrC,370nm}$/OC indicated that primary biomass burning emissions can produce intense light-absorbing BrC, while the photochemical aging process may weaken the light-absorbing capability of BrC.

Using a radiative transfer model (i.e., SBDART), we estimated the BrC effects on aerosol radiative forcing. The average shortwave aerosol direct radiative forcings due to scattering, BrC absorption, and BC absorption at the TOA were evaluated to be -21.4±5.5 W m^{-2}, 2.3±1.8 W m^{-2}, and 10.9±5.1 W m^{-2}, respectively. BrC absorption accounted for 15.8±4.4% of the total shortwave solar absorption warming effect at the TOA, indicating that BrC might be an important climate forcing agent, which is largely neglected in current climate models. To facilitate the estimation of the climate effects of BrC, a set of look-up charts was constructed for the investigated area based on the default tropical atmosphere profile, average surface albedo, average asymmetry factor, and surface-measured aerosol properties (i.e., BrC absorption contribution, *SSA*, and AOD). Therefore, the role of the BrC radiative forcing efficiency at three wavelengths can be conveniently assessed for certain *SSA* and BrC absorption contributions.

Author contributions

HT, JZ, YM, and CC designed the experiments, and ZL, LL, YQ, NW, FL, YL, and MC carried out the field measurements and data analysis. ZL and YQ performed Mie theory simulation. ZL, JZ, and HT prepared the manuscript with comments from all coauthors.

Acknowledgements

This work is supported by the National Key Project of MOST (2016YFC0201901 and 2016YFC0203305), and National Natural Science Foundation of China (41575122 and 41730106). We are also deeply thankful for Dr. Wu and the staff at the Hong Kong Polytechnic University site of AERONET.

References:

Andreae, M. O., and Merlet, P.: Emission of trace gases and aerosols from biomass burning, Glob. Biogeochem. Cycle, 15, 955-966, 2001.

Andreae, M. O., and Gelencser, A.: Black carbon or brown carbon? The nature of light-absorbing carbonaceous aerosols, Atmospheric Chemistry & Physics, 6, 3131-3148, 2006.

Ångström, A.: On the Atmospheric Transmission of Sun Radiation and on Dust in the Air, Geografiska Annaler, 11, 156-166, 1929.

Arnott, W. P., Hamasha, K., Moosmüller, H., Sheridan, P. J., and Ogren, J. A.: Towards Aerosol Light-Absorption Measurements with a 7-Wavelength Aethalometer: Evaluation with a Photoacoustic Instrument and 3-Wavelength Nephelometer, Aerosol Science and Technology, 39, 17-29, 10.1080/027868290901972, 2005.

Arola, A., Schuster, G. L., Pitkänen, M. R. A., Dubovik, O., Kokkola, H., Lindfors, A. V., Mielonen, T., Raatikainen, T., Romakkaniemi, S., Tripathi, S. N., and Lihavainen, H.: Direct radiative effect by brown carbon over the Indo-Gangetic Plain, Atmospheric Chemistry and Physics, 15, 12731-12740, 10.5194/acp-15-12731-2015, 2015.

Bauer, J. J., Yu, X.-Y., Cary, R., Laulainen, N., and Berkowitz, C.: Characterization of the Sunset Semi-Continuous Carbon Aerosol Analyzer, Journal of the Air & Waste Management Association, 59, 826-833, 10.3155/1047-3289.59.7.826, 2012.

Bodhaine, B. A.: Aerosol absorption measurements at Barrow, Mauna Loa and the south pole, Journal of Geophysical Research Atmospheres, 100, 8967–8975, 1995.

698 Bohren, C. F., and Huffman, D. R.: Wiley: Absorption and Scattering of Light by Small
699 Particles - Craig F. Bohren, Donald R. Huffman, Optics & Laser Technology, 31, 328-328, 1983.

700 Bohren, C. F., and Huffman, D. R.: Absorption and Scattering of Light by Small Particles,
701 WILEY‐VCH Verlag GmbH & Co. KGaA 328-328 pp., 2007.

702 Bond, T. C., Streets, D. G., Yarber, K. F., Nelson, S. M., Woo, J. H., and Klimont, Z.: A
703 technology-based global inventory of black and organic carbon emissions from combustion, J.
704 Geophys. Res.-Atmos., 109, 43, 10.1029/2003jd003697, 2004.

705 Bond, T. C., Zarzycki, C., Flanner, M. G., and Koch, D. M.: Quantifying immediate radiative
706 forcing by black carbon and organic matter with the Specific Forcing Pulse, Atmospheric
707 Chemistry and Physics, 11, 1505-1525, 10.5194/acp-11-1505-2011, 2011.

708 Bricaud, A., and Morel, A.: Light attenuation and scattering by phytoplanktonic cells: a
709 theoretical modeling, Applied Optics, 25, 571, 10.1364/ao.25.000571, 1986.

710 Burling, I. R., Yokelson, R. J., Akagi, S. K., Urbanski, S. P., Wold, C. E., Griffith, D. W. T.,
711 Johnson, T. J., Reardon, J., and Weise, D. R.: Airborne and ground-based measurements of the
712 trace gases and particles emitted by prescribed fires in the United States (vol 11, pg 12197,
713 2011), Atmospheric Chemistry and Physics, 12, 103-103, 10.5194/acp-12-103-2012, 2012.

714 Chan, C. K., and Yao, X.: Air pollution in mega cities in China, Atmospheric Environment, 42,
715 1-42, http://dx.doi.org/10.1016/j.atmosenv.2007.09.003, 2008.

716 Cheng, Y., He, K. B., Zheng, M., Duan, F. K., Du, Z. Y., Ma, Y. L., Tan, J. H., Yang, F. M., Liu,
717 J. M., Zhang, X. L., Weber, R. J., Bergin, M. H., and Russell, A. G.: Mass absorption efficiency
718 of elemental carbon and water-soluble organic carbon in Beijing, China, Atmospheric
719 Chemistry and Physics, 11, 11497-11510, 10.5194/acp-11-11497-2011, 2011.

720 Cheng, Y. F., Eichler, H., Wiedensohler, A., Heintzenberg, J., Zhang, Y. H., Hu, M., Herrmann,
721 H., Zeng, L. M., Liu, S., Gnauk, T., Brüggemann, E., and He, L. Y.: Mixing state of elemental
722 carbon and non-light-absorbing aerosol components derived from in situ particle optical
723 properties at Xinken in Pearl River Delta of China, Journal of Geophysical Research:
724 Atmospheres, 111, doi:10.1029/2005JD006929, 2006.

725 Cheung, H. H. Y., Tan, H., Xu, H., Li, F., Wu, C., Yu, J. Z., and Chan, C. K.: Measurements of
726 non-volatile aerosols with a VTDMA and their correlations with carbonaceous aerosols in
727 Guangzhou, China, Atmospheric Chemistry and Physics, 16, 8431-8446, 10.5194/acp-16-
728 8431-2016, 2016.

729 Coen, M. C., Weingartner, E., Apituley, A., Ceburnis, D., Fierzschmidhauser, R., Flentje, H.,
730 Henzing, J. S., Jennings, S. G., Moerman, M., and Petzold, A.: Minimizing light absorption
731 measurement artifacts of the Aethalometer: evaluation of five correction algorithms,
732 Atmospheric Measurement Techniques, 3, 457-474, 2010.

733 Desyaterik, Y., Sun, Y., Shen, X., Lee, T., Wang, X., Wang, T., and Collett, J. L.: Speciation of

734 “brown” carbon in cloud water impacted by agricultural biomass burning in eastern China,
735 Journal of Geophysical Research: Atmospheres, 118, 7389-7399, 10.1002/jgrd.50561, 2013.

736 Drinovec, L., Močnik, G., Zotter, P., Prévôt, A. S. H., Ruckstuhl, C., Coz, E., Rupakheti, M.,
737 Sciare, J., Müller, T., Wiedensohler, A., and Hansen, A. D. A.: The "dual-spot" Aethalometer:
738 an improved measurement of aerosol black carbon with real-time loading compensation,
739 Atmospheric Measurement Techniques, 8, 1965-1979, 10.5194/amt-8-1965-2015, 2015.

740 Erlick, C., Abbatt, J. P. D., and Rudich, Y.: How Different Calculations of the Refractive Index
741 Affect Estimates of the Radiative Forcing Efficiency of Ammonium Sulfate Aerosols, Journal
742 of the Atmospheric Sciences, 68, 1845-1852, 10.1175/2011jas3721.1, 2011.

743 Feng, X., Dang, Z., Huang, W., Shao, L., and Li, W.: Microscopic morphology and size
744 distribution of particles in PM2.5 of Guangzhou City, J Atmos Chem, 64, 37-51,
745 10.1007/s10874-010-9169-7, 2010.

746 Feng, Y., Ramanathan, V., and Kotamarthi, V. R.: Brown carbon: a significant atmospheric
747 absorber of solar radiation?, Atmospheric Chemistry and Physics, 13, 8607-8621, 10.5194/acp-
748 13-8607-2013, 2013.

749 Hoffer, A., Gelencsér, A., Guyon, P., and Kiss, G.: Optical properties of humic-like substances
750 (HULIS) in biomass-burning aerosols, Atmospheric Chemistry & Physics, 5, 3563-3570, 2005.

751 Holben, B. N., Eck, T. F., Slutsker, I., Tanré, D., Buis, J. P., Setzer, A., Vermote, E., Reagan, J.
752 A., Kaufman, Y. J., and Nakajima, T.: AERONET—A Federated Instrument Network and Data
753 Archive for Aerosol Characterization, Remote Sensing of Environment, 66, 1-16, 1998.

754 Huang, R.-J., Zhang, Y., Bozzetti, C., Ho, K.-F., Cao, J.-J., Han, Y., Daellenbach, K. R., Slowik,
755 J. G., Platt, S. M., Canonaco, F., Zotter, P., Wolf, R., Pieber, S. M., Bruns, E. A., Crippa, M.,
756 Ciarelli, G., Piazzalunga, A., Schwikowski, M., Abbaszade, G., Schnelle-Kreis, J.,
757 Zimmermann, R., An, Z., Szidat, S., Baltensperger, U., Haddad, I. E., and Prévôt, A. S. H.:
758 High secondary aerosol contribution to particulate pollution during haze events in China,
759 Nature, 514, 218-222, 10.1038/nature13774, 2014.

760 Jiang, D., Wang, C., Wu, D., Deng, X., Huang, X., Tan, H., Li, F., and Deng, T.: Diurnal
761 variation of atmospheric boundary layer over Wushan station, Guangzhou using wind profiler
762 radar (in Chinese), Journal of Tropical Meteorology, 29, 129-135, 2013.

763 Jung, J., Lee, H., Kim, Y. J., Liu, X., Zhang, Y., Gu, J., and Fan, S.: Aerosol chemistry and the
764 effect of aerosol water content on visibility impairment and radiative forcing in Guangzhou
765 during the 2006 Pearl River Delta campaign, Journal of Environmental Management, 90, 3231-
766 3244, http://dx.doi.org/10.1016/j.jenvman.2009.04.021, 2009.

767 Katrinak, K. A., Rez, P., Perkes, P. R., and Buseck, P. R.: Fractal geometry of carbonaceous
768 aggregates from an urban aerosol, Environmental Science & Technology, 27, págs. 225-238,
769 1993.

770 Khalizov, A. F., Xue, H., Wang, L., Zheng, J., and Zhang, R.: Enhanced light absorption and
771 scattering by carbon soot aerosol internally mixed with sulfuric acid, The journal of physical
772 chemistry. A, 113, 1066-1074, 10.1021/jp807531n, 2009.

773 Kirchstetter, T. W., Novakov, T., and Hobbs, P. V.: Evidence that the spectral dependence of
774 light absorption by aerosols is affected by organic carbon, Journal of Geophysical Research:
775 Atmospheres, 109, n/a-n/a, 10.1029/2004jd004999, 2004.

776 Kulkarni, P., Baron, P. A., and Willeke, K.: Aerosol measurement : principles, techniques, and
777 applications, Van Nostrand Reinhold, 807-808 pp., 1996.

778 Lack, D. A., and Cappa, C. D.: Impact of brown and clear carbon on light absorption
779 enhancement, single scatter albedo and absorption wavelength dependence of black carbon,
780 Atmospheric Chemistry and Physics, 10, 4207-4220, 10.5194/acp-10-4207-2010, 2010.

781 Lack, D. A., and Langridge, J. M.: On the attribution of black and brown carbon light absorption
782 using the Ångström exponent, Atmospheric Chemistry and Physics, 13, 10535-10543,
783 10.5194/acp-13-10535-2013, 2013.

784 Lai, S.-c., Zou, S.-c., Cao, J.-j., Lee, S.-c., and Ho, K.-f.: Characterizing ionic species in PM2.5
785 and PM10 in four Pearl River Delta cities, South China, Journal of Environmental Sciences, 19,
786 939-947, https://doi.org/10.1016/S1001-0742(07)60155-7, 2007.

787 Laskin, A., Laskin, J., and Nizkorodov, S. A.: Chemistry of atmospheric brown carbon, Chem
788 Rev, 115, 4335-4382, 10.1021/cr5006167, 2015.

789 Lee, E., Chan, C. K., and Paatero, P.: Application of positive matrix factorization in source
790 apportionment of particulate pollutants in Hong Kong, Atmospheric Environment, 33, 3201-
791 3212, https://doi.org/10.1016/S1352-2310(99)00113-2, 1999.

792 Levine, J.: Biomass Burning Aerosols in a Savanna Region of the Ivory Coast, French Forum,
793 235-236, 1991.

794 Li, H., Han, Z., Cheng, T., Du, H., Kong, L., Chen, J., Zhang, R., and Wang, W.: Agricultural
795 Fire Impacts on the Air Quality of Shanghai during Summer Harvesttime, Aerosol and Air
796 Quality Research, 10.4209/aaqr.2009.08.0049, 2010.

797 Lin, P., Hu, M., Deng, Z., Slanina, J., Han, S., Kondo, Y., Takegawa, N., Miyazaki, Y., Zhao,
798 Y., and Sugimoto, N.: Seasonal and diurnal variations of organic carbon in PM2.5in Beijing
799 and the estimation of secondary organic carbon, Journal of Geophysical Research, 114,
800 10.1029/2008jd010902, 2009.

801 Liu, C., Chung, C. E., Yin, Y., and Schnaiter, M.: The absorption Ångström exponent of black
802 carbon: from numerical aspects, Atmospheric Chemistry and Physics, 18, 6259-6273,
803 10.5194/acp-18-6259-2018, 2018.

804 Liu, D., Taylor, J. W., Young, D. E., Flynn, M. J., Coe, H., and Allan, J. D.: The effect of

complex black carbon microphysics on the determination of the optical properties of brown carbon, Geophysical Research Letters, 42, 613-619, 2015.

Liu, L., Mishchenko, M. I., and Patrick Arnott, W.: A study of radiative properties of fractal soot aggregates using the superposition T-matrix method, Journal of Quantitative Spectroscopy and Radiative Transfer, 109, 2656-2663, 10.1016/j.jqsrt.2008.05.001, 2008.

Ma, N., Zhao, C. S., Müller, T., Cheng, Y. F., Liu, P. F., Deng, Z. Z., Xu, W. Y., Ran, L., Nekat, B., van Pinxteren, D., Gnauk, T., Müller, K., Herrmann, H., Yan, P., Zhou, X. J., and Wiedensohler, A.: A new method to determine the mixing state of light absorbing carbonaceous using the measured aerosol optical properties and number size distributions, Atmos. Chem. Phys., 12, 2381-2397, 10.5194/acp-12-2381-2012, 2012.

Ma, Y., Li, S. Z., Zheng, J., Khalizov, A., Wang, X., Wang, Z., and Zhou, Y. Y.: Size-resolved measurements of mixing state and cloud-nucleating ability of aerosols in Nanjing, China, J. Geophys. Res.-Atmos., 122, 9430-9450, 10.1002/2017jd026583, 2017.

Mie, G.: Beitrage Zur Optik Truber Medien, Speziell Kolloidaler Metallosungen, Annalen Der Physik, 25, 377, 1908.

Moosmüller, H., Chakrabarty, R. K., Ehlers, K. M., and Arnott, W. P.: Absorption Ångström coefficient, brown carbon, and aerosols: basic concepts, bulk matter, and spherical particles, Atmospheric Chemistry and Physics, 11, 1217-1225, 10.5194/acp-11-1217-2011, 2011.

Nakayama, T., Ikeda, Y., Sawada, Y., Setoguchi, Y., Ogawa, S., Kawana, K., Mochida, M., Ikemori, F., Matsumoto, K., and Matsumi, Y.: Properties of light‐absorbing aerosols in the Nagoya urban area, Japan, in August 2011 and January 2012: Contributions of brown carbon and lensing effect, Journal of Geophysical Research Atmospheres, 119, 12,721-712,739, 2015.

Olson, M. R., Victoria Garcia, M., Robinson, M. A., Van Rooy, P., Dietenberger, M. A., Bergin, M., and Schauer, J. J.: Investigation of black and brown carbon multiple-wavelength-dependent light absorption from biomass and fossil fuel combustion source emissions, Journal of Geophysical Research: Atmospheres, 120, 6682-6697, 10.1002/2014jd022970, 2015.

Pio, C. A., Legrand, M., Alves, C. A., Oliveira, T., Afonso, J., Caseiro, A., Puxbaum, H., Sanchez-Ochoa, A., and Gelencsér, A.: Chemical composition of atmospheric aerosols during the 2003 summer intense forest fire period, Atmospheric Environment, 42, 7530-7543, 2008.

Qin, Y. M., Tan, H. B., Li, Y. J., Li, Z. J., Schurman, M. I., Liu, L., Wu, C., and Chan, C. K.: Chemical characteristics of brown carbon in atmospheric particles at a suburban site near Guangzhou, China, Atmospheric Chemistry and Physics Discussions, 1-23, 10.5194/acp-2018-730, 2018.

Redmond, H., and Thompson, J. E.: Evaluation of a quantitative structure-property relationship (QSPR) for predicting mid-visible refractive index of secondary organic aerosol (SOA), Physical chemistry chemical physics : PCCP, 13, 6872-6882, 10.1039/c0cp02270e, 2011.

Ricchiazzi, P., Yang, S., Gautier, C., and Sowle, D.: SBDART: A Research and Teaching Software Tool for Plane-Parallel Radiative Transfer in the Earth's Atmosphere, Bulletin of the American Meteorological Society, 79, 2101-2114, 10.1175/1520-0477(1998)079<2101:Sarats>2.0.Co;2, 1998.

Roesch, A.: Use of Moderate-Resolution Imaging Spectroradiometer bidirectional reflectance distribution function products to enhance simulated surface albedos, Journal of Geophysical Research, 109, 10.1029/2004jd004552, 2004.

Sareen, N., Schwier, A. N., Shapiro, E. L., Mitroo, D., and McNeill, V. F.: Secondary organic material formed by methylglyoxal in aqueous aerosol mimics, Atmospheric Chemistry and Physics, 10, 997-1016, 10.5194/acp-10-997-2010, 2010.

Satish, R., Shamjad, P., Thamban, N., Tripathi, S., and Rastogi, N.: Temporal Characteristics of Brown Carbon over the Central Indo-Gangetic Plain, Environ Sci Technol, 51, 6765-6772, 10.1021/acs.est.7b00734, 2017.

Scarnato, B. V., Nielsen, K., Vahidinia, S., and Richard, D.: Effect of Aggregation and Mixing on optical properties of Black Carbon, 2013.

Schmid, O., Artaxo, P., Arnott, W. P., Chand, D., Gatti, L. V., Frank, G. P., Hoffer, A., Schnaiter, M., and Andreae, M. O.: Spectral light absorption by ambient aerosols influenced by biomass burning in the Amazon Basin. I: Comparison and field calibration of absorption measurement techniques, Atmos. Chem. Phys., 6, 3443-3462, 10.5194/acp-6-3443-2006, 2006.

Segura, S., Estellés, V., Titos, G., Lyamani, H., Utrillas, M. P., Zotter, P., Prévôt, A. S. H., Močnik, G., Alados-Arboledas, L., and Martínez-Lozano, J. A.: Determination and analysis of in situ spectral aerosol optical properties by a multi-instrumental approach, Atmospheric Measurement Techniques, 7, 2373-2387, 10.5194/amt-7-2373-2014, 2014.

Seinfeld, J. H., and Pandis, S. N.: Atmospheric Chemistry and Physics, John Wiley & Sons, Inc, New York, 1998.

Stokes, G. M., and Schwartz, S. E.: The Atmospheric Radiation Measurement (ARM) Program: Programmatic Background and Design of the Cloud and Radiation Test Bed, Bulletin of the American Meteorological Society, 75, 1201–1221, 1994.

T. C. Bond, †, M. Bussemer, B. Wehner, S. Keller, R. J. Charlson, a., and Heintzenberg‡, J.: Light Absorption by Primary Particle Emissions from a Lignite Burning Plant, Environmental Science & Technology, 33, 3887-3891, 1999.

Tan, H., Liu, L., Fan, S., Li, F., Yin, Y., Cai, M., and Chan, P. W.: Aerosol optical properties and mixing state of black carbon in the Pearl River Delta, China, Atmospheric Environment, 131, 196-208, http://dx.doi.org/10.1016/j.atmosenv.2016.02.003, 2016a.

Tan, H., Yin, Y., Li, F., Liu, X., Chan, P. W., Deng, T., Deng, X., Wan, Q., and Wu, D.: Measurements of particle number size distributions and new particle formations events during

winter in the Pearl River Delta region, China, Journal of Tropical Meteorology, 22, 191-199, 10.16555/j.1006-8775.2016.02.009, 2016b.

Waldman, J. M., Lioy, P. J., Zelenka, M., Jing, L., Lin, Y. N., He, Q. C., Qian, Z. M., Chapman, R., and Wilson, W. E.: Wintertime measurements of aerosol acidity and trace elements in Wuhan, a city in central China, Atmospheric Environment. Part B. Urban Atmosphere, 25, 113-120, https://doi.org/10.1016/0957-1272(91)90045-G, 1991.

Wang, J., Nie, W., Cheng, Y., Shen, Y., Chi, X., Wang, J., Huang, X., Xie, Y., Sun, P., Xu, Z., Qi, X., Su, H., and Ding, A.: Light absorption of brown carbon in eastern China based on 3-year multi-wavelength aerosol optical property observations and an improved absorption Ångström exponent segregation method, Atmospheric Chemistry and Physics, 18, 9061-9074, 10.5194/acp-18-9061-2018, 2018.

Washenfelder, R. A., Attwood, A. R., Brock, C. A., Guo, H., Xu, L., Weber, R. J., Ng, N. L., Allen, H. M., Ayres, B. R., and Baumann, K.: Biomass burning dominates brown carbon absorption in the rural southeastern United States, Geophysical Research Letters, 42, 653-664, 2015.

Wex, H., Neusüß, C., Wendisch, M., Stratmann, F., Koziar, C., Keil, A., Wiedensohler, A., and Ebert, M.: Particle scattering, backscattering, and absorption coefficients: An in situ closure and sensitivity study, Journal of Geophysical Research Atmospheres, 107, LAC-1-LAC 4-18, 2002.

Wu, C., Wu, D., and Yu, J. Z.: Quantifying black carbon light absorption enhancement with a novel statistical approach, Atmospheric Chemistry and Physics, 18, 289-309, 10.5194/acp-18-289-2018, 2018.

Wu, D., Mao, J., Deng, X., Tie, X., Zhang, Y., Zeng, L., Li, F., Tan, H., Bi, X., Huang, X., Chen, J., and Deng, T.: Black carbon aerosols and their radiative properties in the Pearl River Delta region, Science in China Series D: Earth Sciences, 52, 1152-1163, 10.1007/s11430-009-0115-y, 2009.

Xie, C., Xu, W., Wang, J., Wang, Q., Liu, D., Tang, G., Chen, P., Du, W., Zhao, J., Zhang, Y., Zhou, W., Han, T., Bian, Q., Li, J., Fu, P., Wang, Z., Ge, X., Allan, J., Coe, H., and Sun, Y.: Vertical characterization of aerosol optical properties and brown carbon in winter in urban Beijing, China, Atmospheric Chemistry and Physics Discussions, 1-28, 10.5194/acp-2018-788, 2018.

Yu, J., Yan, C., Liu, Y., Li, X., Zhou, T., and Zheng, M.: Potassium: A Tracer for Biomass Burning in Beijing?, Aerosol and Air Quality Research, 18, 2447-2459, 10.4209/aaqr.2017.11.0536, 2018.

Yuan, J. F., Huang, X. F., Cao, L. M., Cui, J., Zhu, Q., Huang, C. N., Lan, Z. J., and He, L. Y.: Light absorption of brown carbon aerosol in the PRD region of China, Atmospheric Chemistry and Physics, 16, 1433-1443, 10.5194/acp-16-1433-2016, 2016a.

914 Yuan, L., Yin, Y., Xiao, H., Yu, X., Hao, J., Chen, K., and Liu, C.: A closure study of aerosol
915 optical properties at a regional background mountainous site in Eastern China, Science of The
916 Total Environment, 550, 950-960, 10.1016/j.scitotenv.2016.01.205, 2016b.

917 Zhang, Y., Li, Z., Sun, Y., Lv, Y., and Xie, Y.: Estimation of atmospheric columnar organic
918 matter (OM) mass concentration from remote sensing measurements of aerosol spectral
919 refractive indices, Atmospheric Environment, 179, 107-117, 10.1016/j.atmosenv.2018.02.010,
920 2018.

921 Zhou, S., Wang, T., Wang, Z., Li, W., Xu, Z., Wang, X., Yuan, C., Poon, C. N., Louie, P. K. K.,
922 Luk, C. W. Y., and Wang, W.: Photochemical evolution of organic aerosols observed in urban
923 plumes from Hong Kong and the Pearl River Delta of China, Atmospheric Environment, 88,
924 219-229, 10.1016/j.atmosenv.2014.01.032, 2014.
925
926

Table 1. Inter-comparison of the performance of various Mie-calculation schemes. The base case is based on the empirical distribution function and mixing states of BC particles obtained from previous field measurements at the same site. $\Phi_{N,CV}$ denotes the portion of non-BC particles and r_{ext} is the mass portion of externally mixed BC with respect to total BC. AAE_{BC} is the absorption Ångström exponent of BC, and the subscript represents the wavelength range. $Abs_{BrC,370}$% and $Abs_{BrC,520}$% are the BrC absorption contributions at 370 nm and 520 nm, respectively. $Calcabs_{880}$ is the calculated absorption at 880 nm using Mie model. $Measabs_{880}$ is the measured absorption by an Aethalometer at 880 nm. b is the intercept of the regression analysis between $Measabs_{880}$ and $Calcabs_{880}$, i.e., $Calcabs_{880}$=b* $Measabs_{880}$. R^2 is the correlation coefficient of the equation. The refractive index of BC core ($\widetilde{m}_{core}$) and nonlight-absorbing particles ($\widetilde{m}_{non}$) is set to be 1.80-0.54i and 1.55-10^{-7}i, respectively (Tan et al., 2016a),

Case #	Scheme	$\Phi_{N,CV}$	r_{ext}	$AAE_{BC,370-520}$	$AAE_{BC,520-880}$	$Abs_{BrC,370}$%	$Abs_{BrC,520}$%	$Calcabs_{880}$	$Measabs_{880}$	b	R^2
Base		0.384 to 0.137	0.58	0.723	0.962	34.13%	15.96%	21.869		1.019	0.979
1		0	1	0.331	0.626	51.64%	29.57%	15.832		0.747	0.968
2		0	0	0.856	1.128	24.76%	8.28%	27.827		1.295	0.976
3		0	0.58	0.745	0.974	33.22%	15.46%	21.936	**21.199**	1.029	0.979
4		0.384 to 0.137	0	0.835	1.111	26.01%	9.14%	27.302		1.269	0.975
5		0.5	0	0.778	1.043	29.96%	12.30%	24.921		1.150	0.968
6		0.5	0.58	0.674	0.928	36.39%	17.49%	20.897		0.977	0.975

941 **Table 2.** Observational studies of the BrC light absorption coefficient and contribution in the
942 near-ultraviolet wavelength range in East Asia.

Periods	Location	λ (nm)	Mean BrC absorption coefficient	Mean BrC absorption contribution	Instrumentation	Reference
Nov. 2014 – Jan. 2015	Guangzhou (China)	370	17.6 Mm^{-1} 23.5 Mm^{-1}	26.2% (AAE_{BC}=1) 34.1% (corrected)	Aethalometer AE-33	This study
Jan. 2014 – Feb. 2014; Sep. 2014 – Oct. 2014	Shenzhen (China)	405	3.0 Mm^{-1} 1.4 Mm^{-1}	11.7% (winter) 6.3% (fall)	PASS-3	Yuan et al. (2016a)
Nov. 2014	Heshan (China)	405	3.9 Mm^{-1}	12.1%	PASS-3	Yuan et al. (2016a)
Nov. 2016– Dec. 2016	Beijing (China)	370	106.4 Mm^{-1} 93.8 Mm^{-1}	46% (at the ground) 48% (at 260 m)	Aethalometer AE-33	Xie et al. (2018)
Jun. 2013 – May. 2016	Nanjing (China)	370	35.8 Mm^{-1}	16.7%	Aethalometer AE-31	Wang et al. (2018)
Jan. 2012	Nagoya (Japan)	405	Not detected	11% (300°C) 17% (400°C)	Thermodenuder PASS-3	(Nakayama et al. (2015))

943

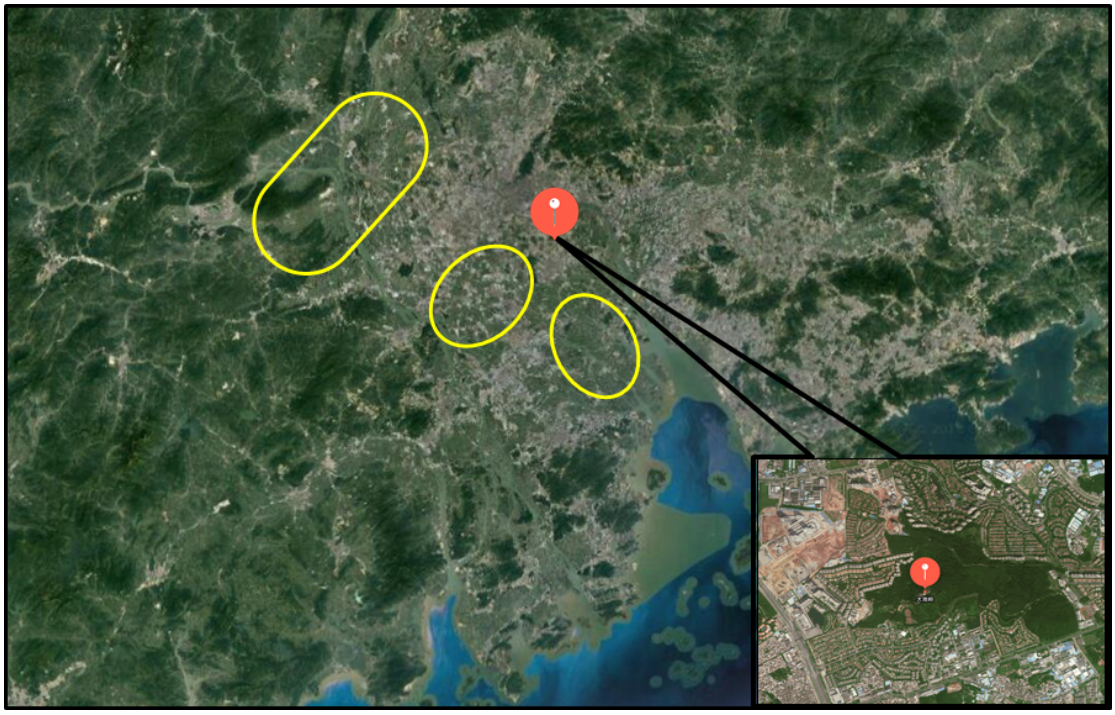

Figure 1. The location of Panyu station (CAWNET) in the PRD region (indicated by the red dot). The plain areas within the yellow circles are the main rural areas of western PRD.

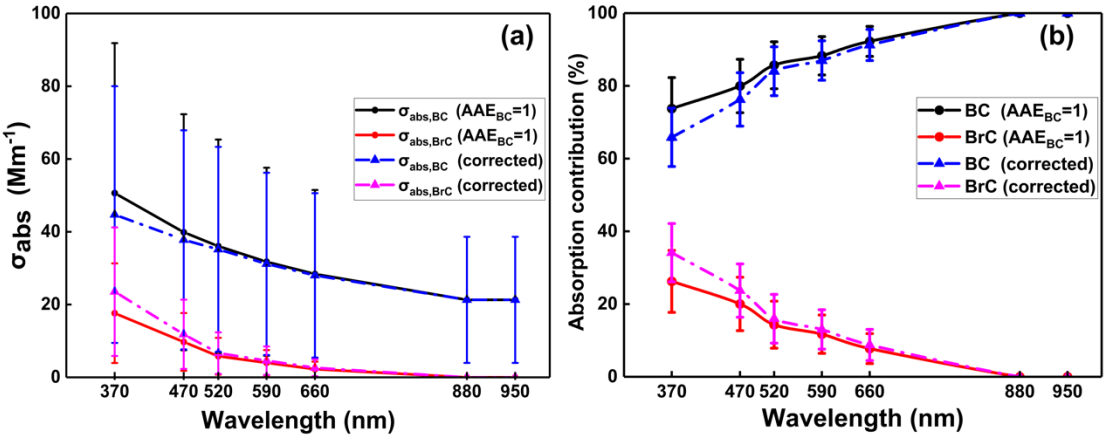

Figure 2. (a) BC and BrC particle average light absorption coefficients at different wavelengths under different AAE_{BC} assumptions; the whiskers represent an error of one standard deviation. (b) Contributions of BC and BrC to the total light absorption coefficient at different wavelengths under different AAE_{BC} assumptions; the whiskers represent an error of one standard deviation.

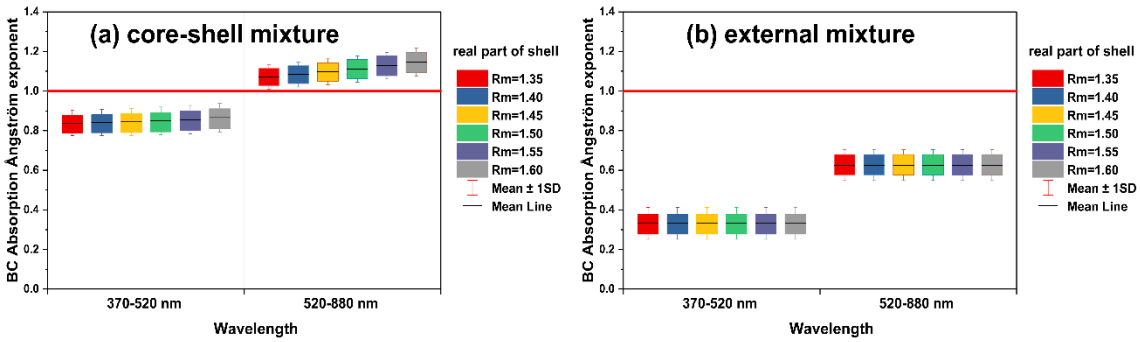

Figure 3. Influence of the wavelength-independent refractive index of the non-absorbing materials on the (a) AAEs of the core-shell mixture and (b) AAEs of the external mixture with a constant BC core refractive index ($\tilde{m}_{core}$=*1.80-0.54i*). The imaginary part of the non(less)-absorbing shell was set to 10^{-7}, while the real part varied from 1.35 to1.60. In each panel, the boundaries of the box represent the 75th and 25th percentiles; the whiskers above and below each box indicate an error of one standard deviation; the black lines in the boxes denote the average values. In panels a and b, the red line indicates where AAE_{BC}=1.

965

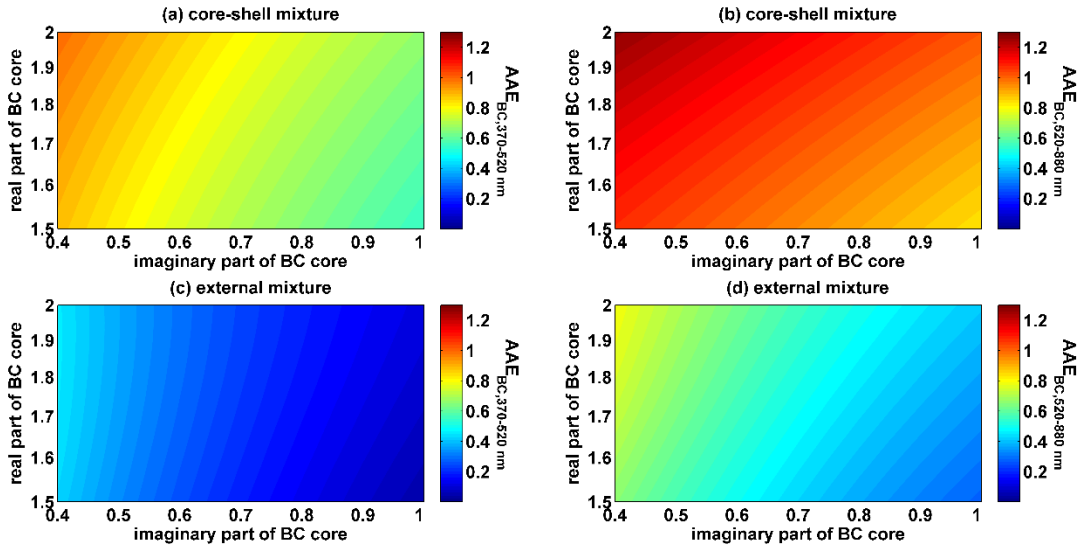

966

967 Figure 4. Influence of the wavelength-independent refractive index of the BC core on
968 AAEs with a constant shell refractive index ($\tilde{m}_{shell}$=*1.55-10*$^{-7}$*i*). A core-shell mixture
969 was used for panels a and b, and an external mixture was used for panels c and d. The
970 real part of $\tilde{m}_{core}$ varied from 1.5 to 2.0, with a step of 0.05, and the imaginary part of
971 $\tilde{m}_{core}$varied from 0.4 to 1.0, with a step of 0.05.

972

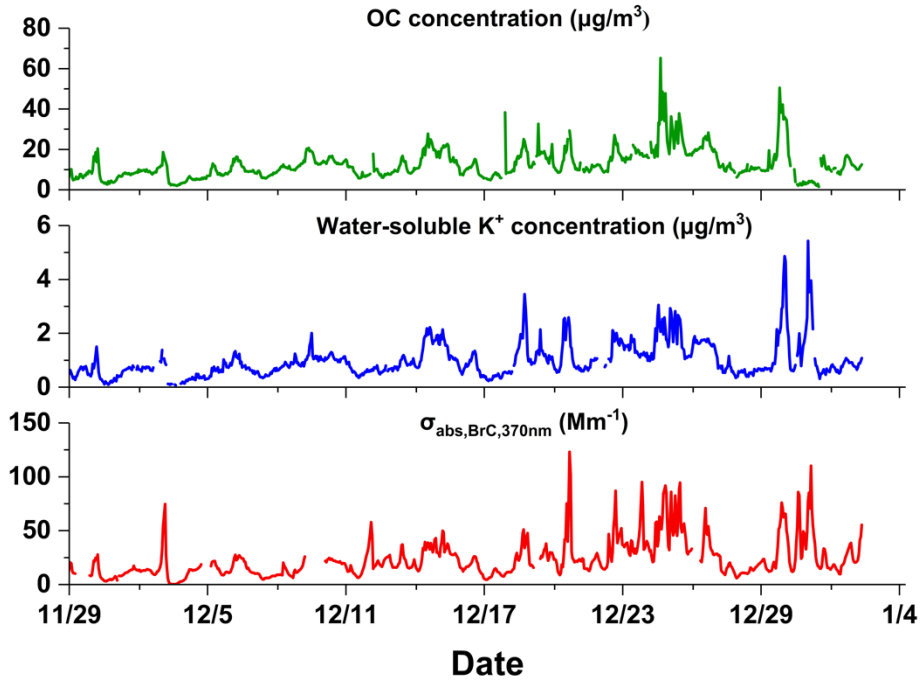

973

974 Figure 5. Time series of the OC aerosol mass concentration (green line), water-soluble K^+ mass

975 concentration (blue line), and BrC light absorption (red line).

976

977

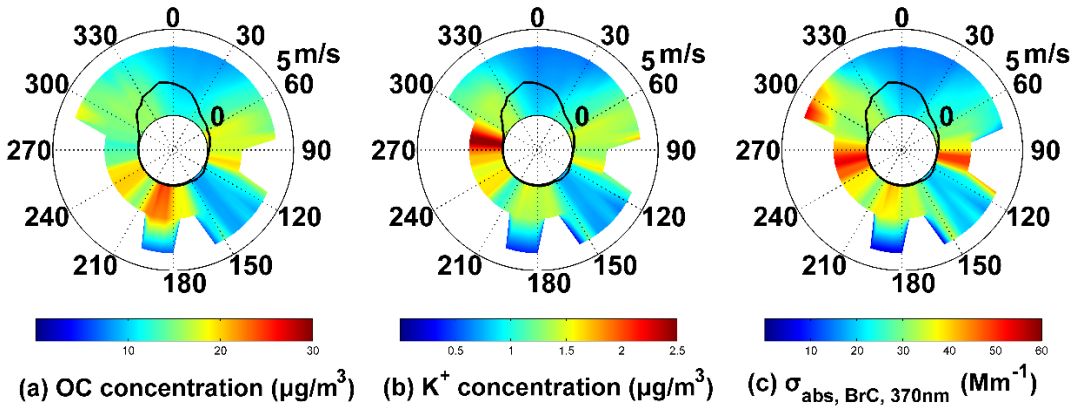

978

979 Figure 6. Wind rose plots of OC (a), K^+ (b), and $\sigma_{abs,BrC,370nm}$ (c). In each panel, the black solid
980 lines denote the frequency of the wind direction. The shaded contour represents the average
981 values of the corresponding species for that wind speed (radial length) and wind direction
982 (transverse direction) in polar coordinates.

983

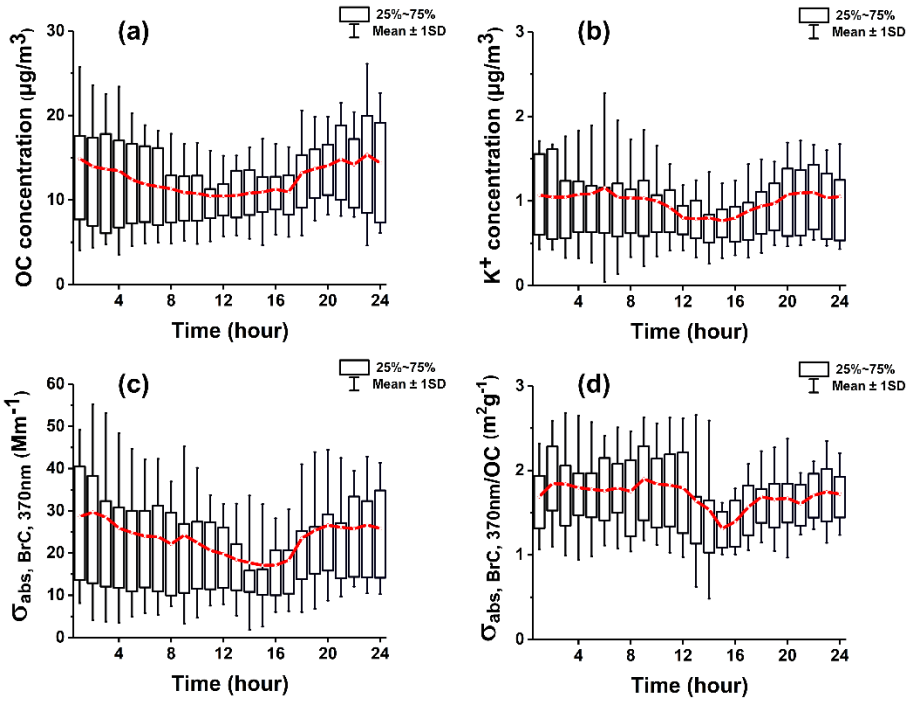

Figure 7. Box-whisker plots of diurnal trends in the OC concentration (a), water-soluble K+ concentration (b), $\sigma_{abs,BrC,370nm}$ (c), and $\sigma_{abs,BrC,370nm}$ /OC (d). The red traces represent the variation in the average value. The upper and lower boundaries of the box represent the 75th and 25th percentiles, respectively; the whiskers above and below each box represent an error of one standard deviation.

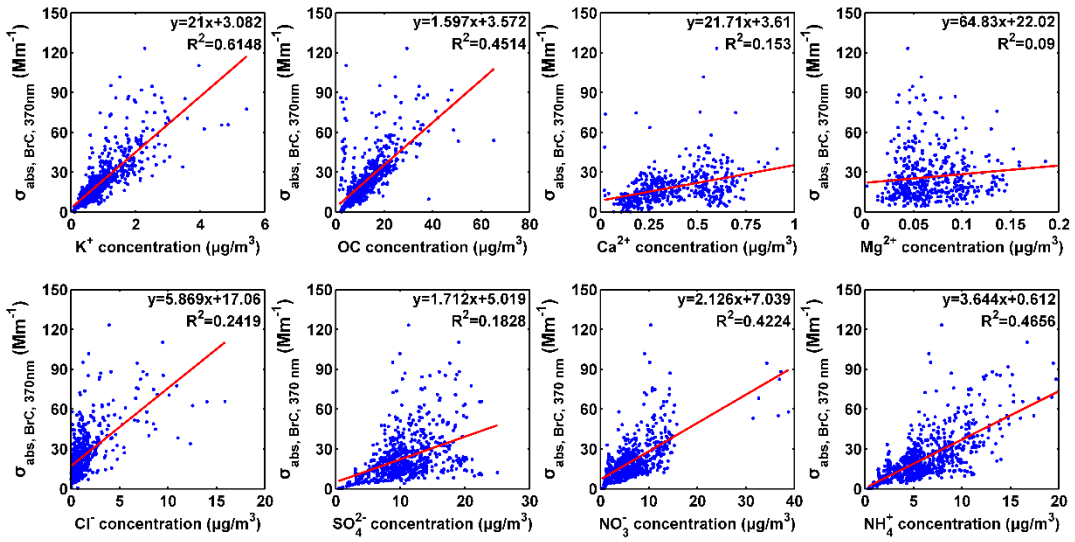

992

993 Figure 8. Correlations of the BrC absorption coefficient at 370 nm with OC, water-soluble K^+,

994 Ca^{2+}, Mg^{2+}, Cl^-, SO_4^{2-}, NO_3^-, and NH_4^+ aerosol concentrations.

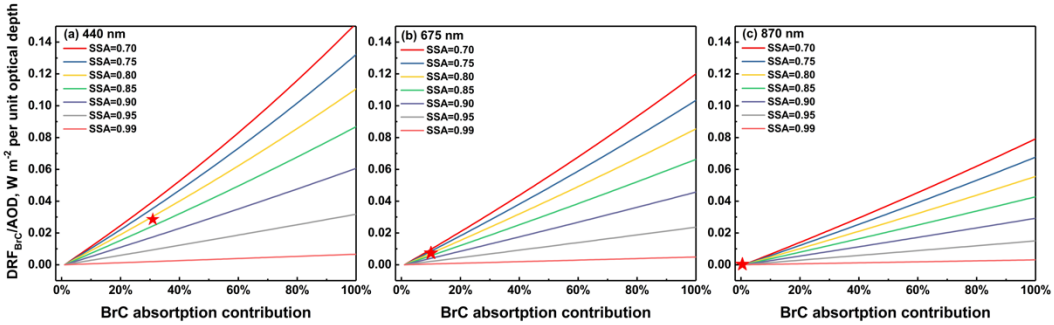

995

996 Figure 9. BrC radiative forcing efficiencies, which are defined as the BrC TOA direct radiative
997 forcing divided by the AOD, as a function of the BrC to BC absorption ratio and *SSA* measured
998 at the surface. The average AOD of the three wavelengths, the average ASY of the three
999 wavelengths, a solar zenith angle of 55°, and average shortwave broadband surface albedo were
1000 used in the calculation. The red star corresponds to the average *SSA* and BrC absorption
1001 contributions determined from this campaign.